LUND UNIVERSITY

Kinematics and Ultraviolet to Infrared Morphology of the Inner Homunculus of Carinae

Smith, Nathan; Morse, Jon A.; Gull, Theodore R.; Hillier, D. John; Gehrz, Robert D.; Walborn, Nolan R.; Bautista, Manuel; Collins, Nicholas R.; Corcoran, Michael F.; Damineli, Augusto; Hamann, Fred; Hartman, Henrik; Johansson, Sveneric; Stahl, Otmar; Weis, Kerstin

Link to publication

KINEMATICS AND ULTRAVIOLET TO INFRARED MORPHOLOGY OF THE INNER HOMUNCULUS OF η CARINAE[1]

NATHAN SMITH,[2,3] JON A. MORSE,[3,4] THEODORE R. GULL,[5] D. JOHN HILLIER,[6] ROBERT D. GEHRZ,[7] NOLAN R. WALBORN,[8] MANUEL BAUTISTA,[9] NICHOLAS R. COLLINS,[5] MICHAEL F. CORCORAN,[10] AUGUSTO DAMINELI,[11] FRED HAMANN,[12] HENRIK HARTMAN,[13] SVENERIC JOHANSSON,[13] OTMAR STAHL,[14] AND KERSTIN WEIS[7,15]

ABSTRACT

We present the first ultraviolet and optical images of η Car and its circumstellar Homunculus nebula, obtained with the Advanced Camera for Surveys/High Resolution Camera (ACS/HRC) on board the *Hubble Space Telescope* (*HST*). Compared to those at visual wavelengths, UV images reveal excess emission 0″.1–0″.6 from the central source along the minor axis that may emanate from the outer parts of η Car's nonspherical stellar wind, which dominates the UV flux from η Car. The UV emission fills the cavity inside a dust torus measured from infrared (IR) data; within 0″.2 of the star the UV emission projects a morphology reminiscent of the IR torus, but it is a factor of 10 smaller. This "little torus" seen in the UV may be related to the "Little Homunculus" discovered recently, signifying recurrent mass ejections with the same geometry. Finally, we reexamine the kinematics of nebular condensations near the star (Weigelt objects C and D) in *HST* images and spectra obtained over the past decade. We measure heliocentric velocities slower than previous estimates, and from proper motions we derive an ejection date of 1908 ± 12 yr, assuming linear motion. However, because of radiative acceleration, these objects may have been ejected earlier—perhaps during the 1890 outburst of η Car.

Subject headings: circumstellar matter — stars: individual (η Carinae) — ultraviolet: stars

1. INTRODUCTION

The recent mass-loss history of η Car, inferred from its complex circumstellar ejecta, provides us with unique insights into the late evolution of the most massive stars. Determining the geometry and ionization structure of the expelled mass is critical for gauging the roles of rotation or close binary interactions in the mass ejection process. With $L \approx 5 \times 10^6 L_\odot$, a current mass that probably exceeds 100 $M_\odot$, extreme vari-

ability, very recent circumstellar ejecta, and a distance of only ~2.3 kpc along a sight line of moderate extinction, η Car is among the most important targets for multiwavelength observations aimed at understanding the fate of very massive stars (e.g., Davidson & Humphreys 1997).

The Homunculus is an elegant bipolar nebula surrounding η Car, with an intricate structure revealed in images taken with the *Hubble Space Telescope* (*HST*) Wide Field Planetary Camera 2 (WFPC2) (Currie et al. 1996; Morse et al. 1998; see also Davidson & Humphreys 1997 for a review of previous studies). It is primarily a dusty reflection nebula (Thackeray 1961; Visvanathan 1967; Hillier & Allen 1992; Schulte-Ladbeck et al. 1999; Smith et al. 2003a) containing several solar masses ejected during η Car's "Great Eruption," which was observed in the mid 19th century (Thackeray 1949; Gaviola 1950; Ringuelet 1958; Gehrz & Ney 1972; Walborn, Blanco, & Thackeray 1978; Currie et al. 1996; Smith & Gehrz 1998; Morse et al. 2001). A ground-based image by Duschl et al. (1995) and WFPC2 images (Morse et al. 1998) showed ragged equatorial debris, some of which may have originated in a circa 1890 eruption (Smith & Gehrz 1998; Davidson et al. 2001). Interesting aspects of the 1890 event were discussed by Walborn & Liller (1977) and Humphreys, Davidson, & Smith (1999).

The two lobes of the Homunculus are mostly hollow, showing clear limb brightening at thermal-infrared (IR) wavelengths (Hackwell, Gehrz, & Grasdalen 1986; Smith et al. 1995, 2002, 2003b; Smith, Gehrz, & Krautter 1998). The polar lobes have diameters of roughly 18,500 AU (~8″) and are expanding at speeds up to 650 km s^{-1} (Meaburn, Wolstencroft, & Walsh 1987, 1993; Hillier & Allen 1992; Davidson et al. 2001). Recent results also reveal complex structure *inside* the Homunculus. Ishibashi et al. (2003) analyzed long-slit spectra obtained with the Space Telescope Imaging Spectrograph (STIS) aboard *HST* and discovered a small bipolar nebula

[2] Hubble Fellow.

[3] Center for Astrophysics and Space Astronomy, University of Colorado, 389 UCB, Boulder, CO 80309; nathans@casa.colorado.edu.

[4] Department of Physics and Astronomy, Arizona State University, Box 871504, Tempe, AZ 85287-1504.

[5] Laboratory of Astronomy and Space Science, NASA-Goddard Space Flight Center, Code 681, Greenbelt, MD 20771.

[6] Department of Physics and Astronomy, University of Pittsburgh, 3941 O'Hara Street, Pittsburgh, PA 15260.

[7] Astronomy Department, University of Minnesota, 116 Church Street SE, Minneapolis, MN 55455.

[8] Space Telescope Science Institute, 3700 San Martin Drive, Baltimore, MD 21218.

[9] Centro de Física, Instituto Venezolano de Investigaciones Científicas, PO Box 21827, Caracas 1020A, Venezuela.

[10] Laboratory for High Energy Astrophysics, NASA-Goddard Space Flight Center, Greenbelt, MD 20771.

[11] Instituto de Astronomia, Geofisica, e Ciencias Atmosfericas, Universidade de São Paulo, Rua do Matao 1226, São Paulo 05508-090, Brazil.

[12] Department of Astronomy, University of Florida, Gainesville, FL 32611.

[13] Atomic Astrophysics, Lund Observatory, Lund University, P.O. Box 43, SE-22100 Lund, Sweden.

[14] Landessternwarte Heidelberg-Königstuhl, Universität Heidelberg, D-69117 Heidelberg, Germany.

[15] Institute of Astronomy, Ruhr-University Bochum, Universitätsstrasse 150, 44780 Bochum, Germany.

expanding at ∼200 km s^{-1} inside the Homunculus, sharing the same polar axis but extending to radii of only ∼4600 AU (2″). Ishibashi et al. suggested that this "Little Homunculus" may have been ejected several decades after the Great Eruption, perhaps in the 1890 event.[16] In addition, IR images have revealed a dust torus inside the Homunculus, with a presumed "rotational" axis tilted at roughly the same inclination as the Homunculus and with a radius of a few thousand AU (Smith et al. 2002, 2003b, and references therein). These interior structures are seen primarily by their line emission from ionized gas in long-slit spectra or by their emission from dust at IR wavelengths that penetrate the thick screen of the Homunculus. They are elusive in WFPC2 images dominated by reflected continuum light, but some of these emission-line structures were revealed by their temporal variability in multiepoch WFPC2 images (Smith et al. 2000). Here we suggest that interior structures are also visible in the UV.

The fine pixel sampling and access to UV wavelengths offered by the High Resolution Camera of the Advanced Camera for Surveys (ACS/HRC) on *HST* provide the best images yet of the inner Homunculus. In this paper we discuss the structure observed in UV and optical *HST* ACS images, which we compare to images at longer wavelengths and *HST* STIS spectra of selected regions. We also discuss the kinematics and ages of the enigmatic "Weigelt objects" that are projected ∼0″2–0″3 from the central source.

2. OBSERVATIONS

The ACS/HRC images presented here are the first observations completed as part of the *HST* Treasury program (PI: K. Davidson; GO-9420) to study η Car and its ejecta during the predicted spectroscopic event of 2003.5 (e.g., Damineli 1996; Damineli, Conti, & Lopes 1997, 1998; Davidson 1997, 1999; Corcoran et al. 1997, 2001; Ishibashi et al. 1999). The ACS/HRC imaging observations are listed in Table 1. Images were obtained in four filters: F220W, F250W, F330W, and F550M. The filter transmission curves are compared to the observed spectrum of η Car in Appendix A, where relative contributions of emission lines and continuum are estimated at several positions.

We applied standard image processing routines to combine individual dithered exposures as described in the *HST* Data Handbook,[17] including cosmic-ray rejection and geometric-distortion correction. The central star was overexposed in the longer integrations in the F220W and F550M filters, so the saturated pixels were masked and replaced with scaled data from the shorter exposure images: this is similar to our

[16] This connection is supported by spectra taken in 1893, which show absorption lines at −180 km s^{-1}, close to the observed expansion speed of the Little Homunculus (see Whitney 1952; Walborn & Liller 1977).

[17] See http://www.stsci.edu/hst/HST_overview/documents/datahandbook.

TABLE 1
ACS/HRC Observation Log (2002 November)

Filter	λ_c (Å)	$\Delta\lambda$ (Å)	Exposure Time
F220W................................	2220	450	4 × 8 s, 4 × 32 s
F250W................................	2650	600	4 × 3 s
F330W................................	3300	550	4 × 1 s
F550M................................	5500	550	4 × 0.3 s, 4 × 2.4 s

Note.—From program GO-9420, Visit 1A, data set J8GM1A*.

processing of WFPC2 images, which included a wide range of exposure times to cover the large dynamic range of η Car and its fainter Homunculus (Morse et al. 1998). The original pixel scale of 0″025 was subdivided, by a factor of 2, to 0″0125 using a standard cubic spline interpolation function. We then applied 10 iterations of the Lucy-Richardson (Lucy 1974; Richardson 1972) deconvolution task LUCY in IRAF, to enhance the spatial resolution and contrast of the images, as was done previously with our WFPC2 data (Morse et al. 1998; Smith et al. 2000). As a sample point-spread function (PSF) for the deconvolution, we used archival ACS/HRC observations of stars in the same four filters, obtained as part of programs GO-9663 and GO-9667. The PSF images were reduced, and the pixel scale was subdivided in exactly the same way as the images of η Car. The final processed images of η Car in all four filters are shown in Figure 1. Figure 2 zooms in on the structure closest to the central star. We achieved point-source spatial resolutions with FWHM values of ∼0″03, 0″03, 0″04, and 0″05 in the F220W, F250W, F330W, and F550M filters, respectively.

In addition, we discuss these new ACS images in context with other imaging data obtained with *HST* and ground-based telescopes at optical and IR wavelengths. Optical *HST* images using the F336W (near-UV continuum + numerous faint emission lines), F631N (red continuum + [S III] λ6312), and F658N ([N II] λ6583 + redshifted Hα) filters obtained with the planetary camera (PC) of WFPC2 over the time interval 1994–2003 (including Treasury program images from 2003 February) are included in our analysis. Most of these observations, along with the data reduction procedures, have been discussed elsewhere (Morse et al. 1998; Smith et al. 2000). Similarly, we incorporate near-IR *HST* NICMOS images obtained in 1998 (Smith & Gehrz 2000) and thermal-IR images obtained in 2001 August with the MIRAC3 camera at the Magellan Observatory (Smith et al. 2002, 2003b).

In our analysis, we incorporate spectroscopic data obtained at various times since 1997 with *HST* STIS as part of programs GO-8036 and 8619.[18] These data give important clues to the kinematics of certain emission structures seen in the images and are discussed in § 3. In § 4 we examine proper motions and radial velocities of the bright Weigelt objects. Appendix A describes how we use additional STIS spectra to evaluate contributions of continuum and emission lines to the imaging filters.

3. EMISSION STRUCTURES INSIDE THE HOMUNCULUS

Fine-scale structures in the Homunculus lobes have been described by Morse et al. (1998) and Schulte-Ladbeck et al. (1999) in their analyses of previous WFPC2 images, and Smith et al. (2000) have discussed temporal photometric variability in WFPC2 data. Here we address wavelength-dependent effects based on the ACS/HRC, WFPC2, and IR data. The finer pixel-sampling of the ACS/HRC provides a modest improvement in spatial resolution over WFPC2 PC data, but the most novel aspect of the new ACS/HRC images is access to UV wavelengths. Figures 1–3 show qualitative differences in wavelength-dependent structure. Figure 4 shows quantitative intensity tracings, Figure 5 presents photometric information, and Figure 6 compares the UV excess to other

[18] See Gull et al. (2001) and Ishibashi et al. (2003) for more detailed descriptions of STIS data acquisition and reduction procedures.
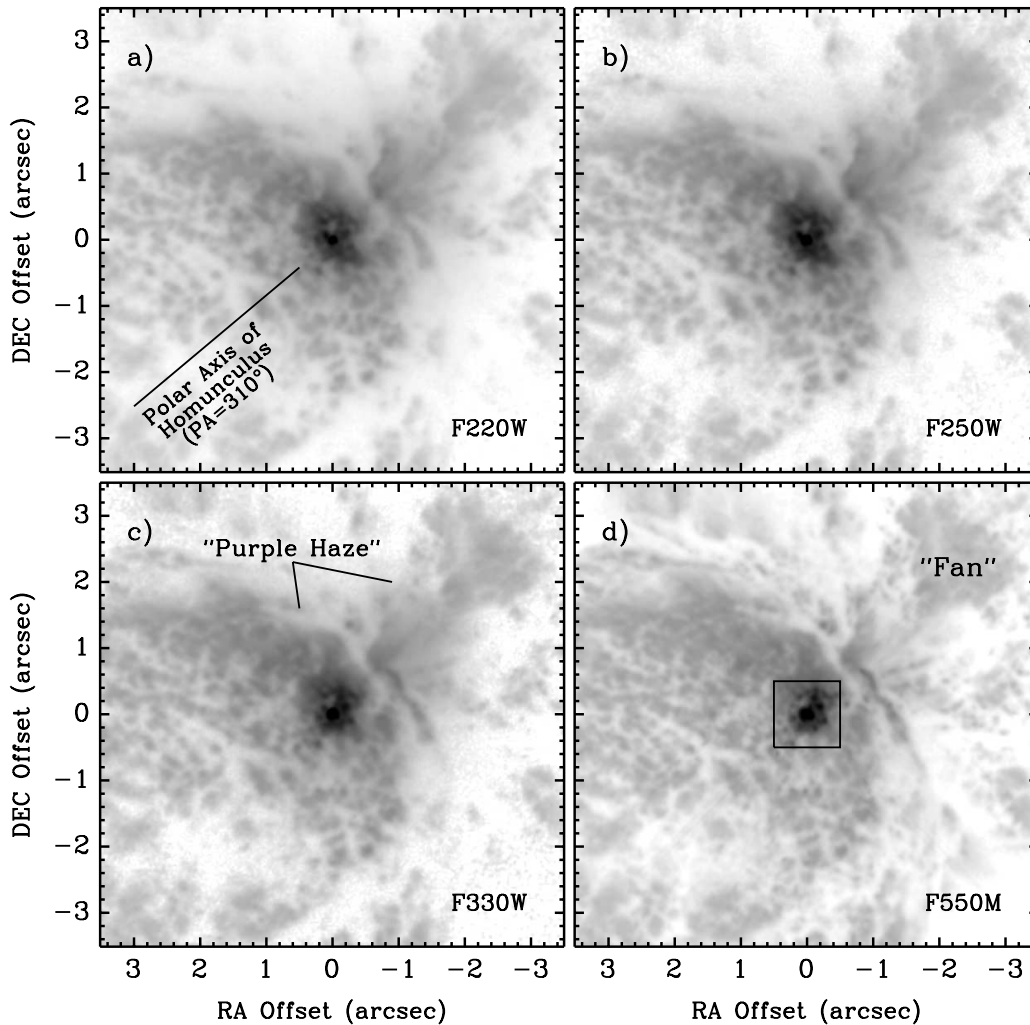
FIG. 1.—Final processed ACS/HRC images of η Car. Only the bright central region of the Homunculus is shown here. The box in (*d*) shows the field of view in Fig. 2.

optical and IR structures. Below we discuss various components of the observed structure in detail.

3.1. *Purple Haze*

Morse et al. (1998) noted large-scale color gradients in the Homunculus, with the outer parts of the nebula appearing more red—possibly as a result of stronger forward-scattering at blue wavelengths. This trend appears to hold in the UV as well (Fig. 4). However, Figures 3 and 4 also reveal locations that are enhanced in the UV much beyond the expected color gradient. One position where the violet and UV emission is relatively stronger than the F550M continuum is in the "Purple Haze" at ∼2″ northwest of the star near the "Fan" (see Figs. 1 and 4*b*). This enhanced emission was noticed in earlier WFPC2 images with the F336W filter (Morse et al. 1998). With the F220W, F250W, and F330W filters, the emission is roughly 4 times stronger than with the F550M continuum filter, relative to the surrounding ejecta (Fig. 4*b*). The fuzzy Purple Haze can be seen in Figures 1, 3, and 6*a*; this region is known to emit numerous narrow emission lines (e.g., Zethson et al. 1999; Davidson et al. 1997). An example of the long-slit STIS spectrum of this region is shown later in Appendix A (Fig. 17). The spectrum shows strong nebular emission lines with complex kinematic structure, typically blueshifted at about −100 km s⁻¹. Figure 17 also includes

emission from some low-ionization filaments near the Purple Haze that emit [Sr II] lines (see Zethson et al. 2001; Hartman et al. 2004). Thus, we conclude that the Purple Haze seen in images is due to intrinsic nebular emission from a patch of diffuse low-ionization gas and not scattered starlight or stellar-wind emission. This is different from the UV excess seen in equatorial regions closer to the star, as discussed below.

3.2. *Extended Equatorial Emission*

Other prominent locations of UV excess emission in Figure 6*a* are seen 0″.1–0″.6 from the star to the northeast and southwest. Figures 1–3, 4*a*, and 6*a* show that with the F220W and F250W filters, bright emission is enhanced along the minor axis of the Homunculus. UV excess emission is not seen along the polar axis near the star in Figure 4*b*. *Could this UV excess simply be due to reduced extinction at these locations?* Figure 6*b* shows that indeed there is lower dust column density here, but several independent facts suggest that lower extinction is *not* solely responsible for the UV excess, despite this coincidence:

1. The high column density of dust that encircles the UV emission (Fig. 6*b*) corresponds to warm dust in a circumstellar torus *inside* the Homunculus (Smith et al. 2003b), and *not* in the cooler foreground lobe. In fact, the apparently low column density at the position of the UV excess is the same as that in
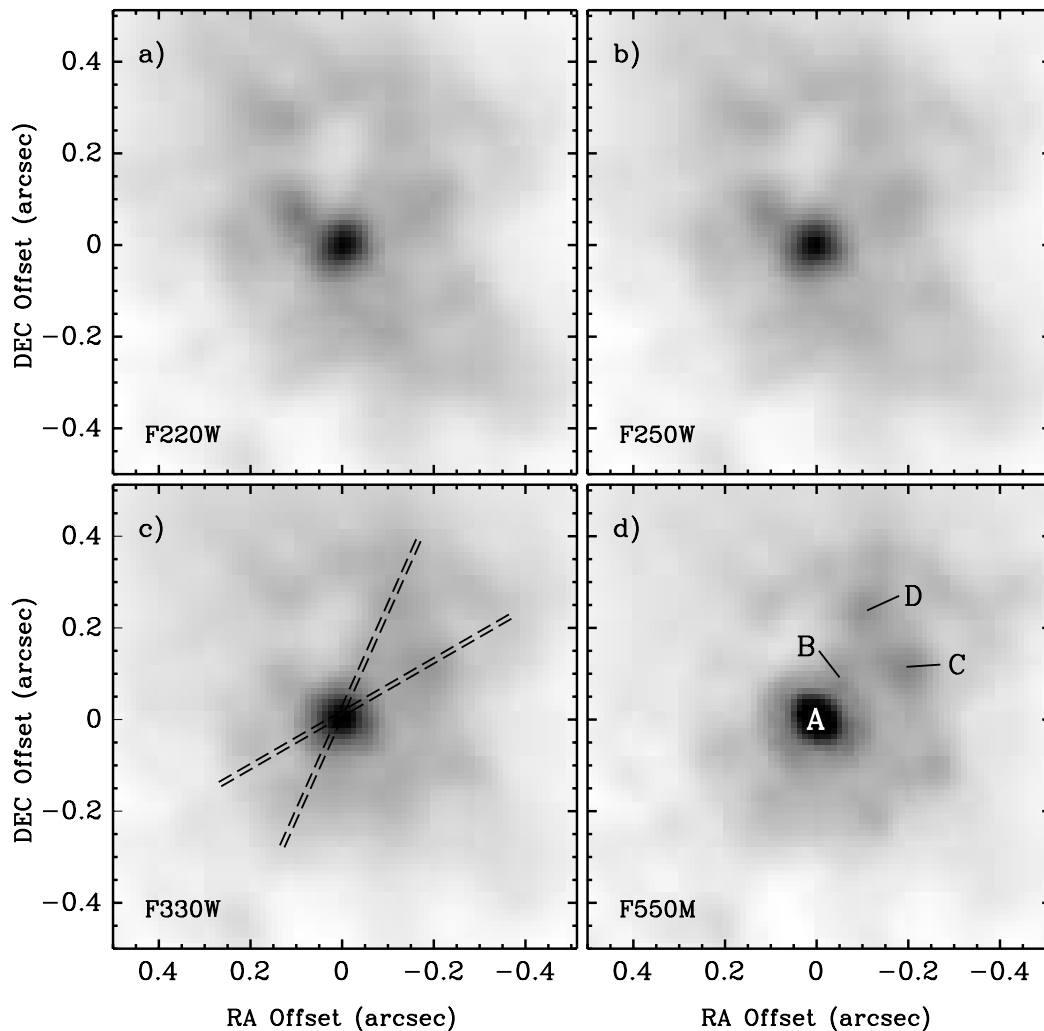
Fig. 2.—Same as Fig. 1, but with a smaller field of view. The Weigelt objects A, B, C, and D are identified in (*d*). The dashed lines in (*c*) represent the directions of intensity tracings through the star and Weigelt objects C and D in Figs. 9 and 10.

the middle of the southeast polar lobe, where the UV excess is absent.

2. At the same locations as the UV excess, nebular emission from [N II] $\lambda6583$ and [S III] $\lambda6312$ is seen in narrowband WFPC2 images (Smith et al. 2000), shown here in Figures 6*c* and 6*d*. If the UV excess were due to a local decrease in wavelength-dependent dust extinction, we should not expect to see red nebular-emission lines confined to the same regions without a corresponding enhancement of the visual/red continuum light.

3. Furthermore, *temporally variable* nebular emission from [S III] and [N II] coincides with the UV excess (Smith et al. 2000). This emission is revealed by temporal variability in a given emission line *at the same wavelength* and is therefore independent of reddening effects

4. High-resolution imaging polarimetry shows strong scattering from the same regions where we see the UV excess (Falcke et al. 1996). Taken together, these arguments suggest that the UV excess is indeed dominated by a real enhancement of the UV emission surrounding the star.

Instead of just nebular emission, the UV excess northeast and southwest of the star may also be scattered light or emission from the outer parts of the stellar wind, presuming that the star has a latitude-dependent radiation field (Smith

et al. 2003a). Figure 5*a* shows photometry measured from the new ACS images of η Car with circular apertures of various radii centered on the star. In the optical continuum traced by the F550M filter, the central star ($r \lesssim 0\farcs05$) contributes $\sim$27% of the total emission within $r < 1\farcs6$, with the rest contributed by reflected light from dust in the Homunculus. At shorter wavelengths, this relative contribution of direct light from the central star decreases to 14% (F330W), 9.5% (F250W), and 8.6% (F220W), signifying that spatially resolved outer parts of the wind contribute a larger fraction of the total UV flux. Far-UV spectra from the *Far Ultraviolet Spectroscopic Explorer* (*FUSE*; Iping et al. 2001) invite a similar conclusion.

Radiative-transfer calculations for the wind of η Car (Hillier et al. 2001; Hillier & Miller 1998) support this conjecture. Figure 5*b* presents two models of emission from η Car's wind: one shows emission contained within a synthetic aperture of radius $0\farcs033$ or $\sim$75 AU (*gray lines*), and the other (*black lines*) shows emission from the rest of the wind outside that radius. These are based on the exact same parameters as for the model fitted to the spectrum of η Car by Hillier et al. (2001), using the same radiative-transfer code (Hillier & Miller 1998).[19] The

---

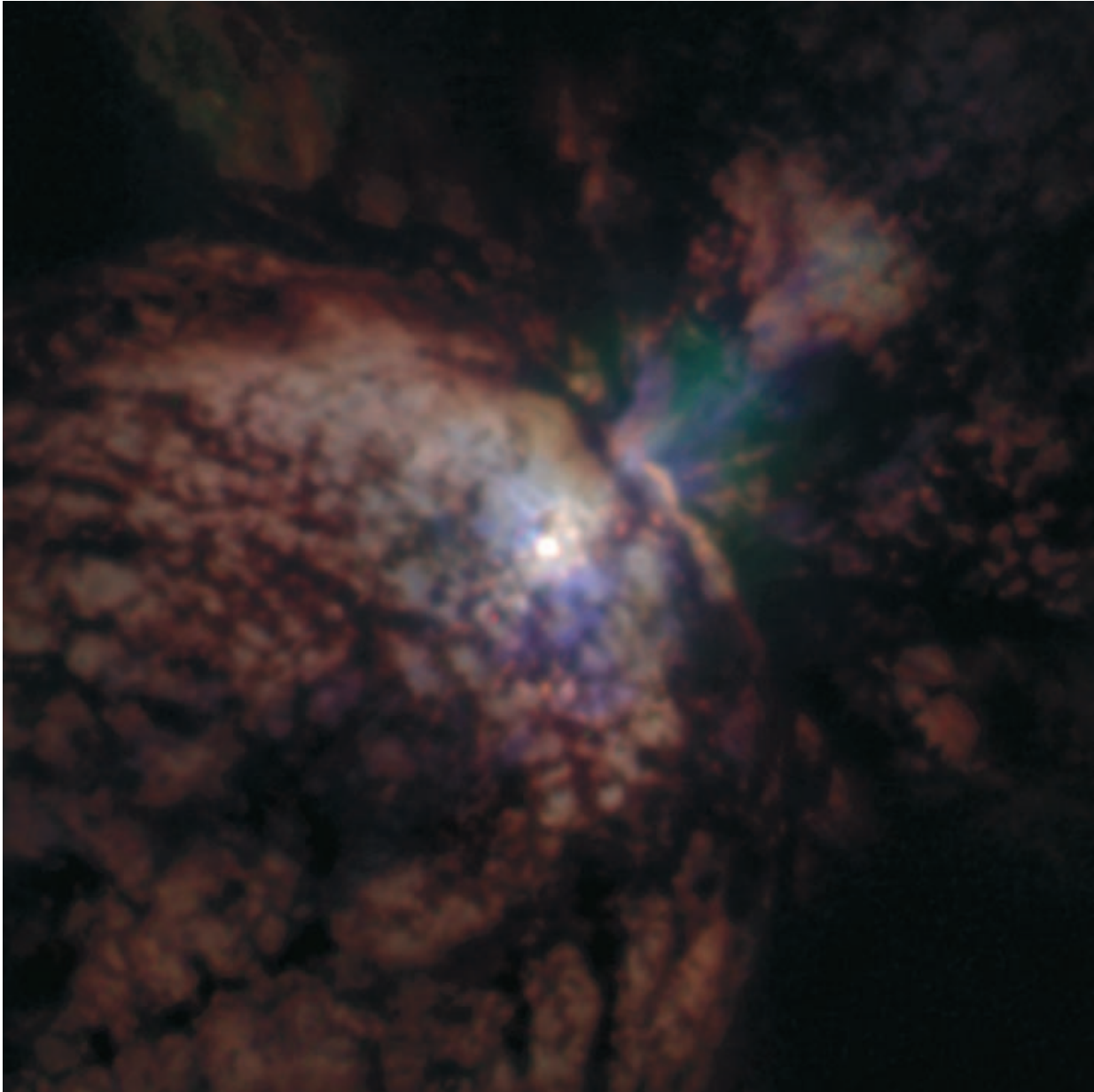[19] The radiative transfer code has been updated to include S, Ti, Cr, Mn, Co, and Ni.

Fɪɢ. 3.—Three-color composite image of the inner core of the Homunculus (same field of view as Fig. 1) with the F220W image in blue, F330W in green, and F550M in red.

gray line showing the simulated spectrum of the central star is essentially the same as in Hillier et al. (2001), and the black line shows emission from the same model but sampling emission from 1000 to 20,000 stellar radii instead. Note the very different shapes of the energy distributions in these two model spectra. Emission from the *outer wind* in these models is much brighter in the UV, relative to the visual-wavelength continuum, which is consistent with the results of our aperture photometry (Fig. 5a) and the shapes of the continua in the star and UV excess shown in Appendix A (Figs. 12, 13, and 16). Thus, these models predict that most of the UV emission at wavelengths shorter than about 3500 Å escapes from outer parts of the wind beyond 75 AU. This can explain why excess emission is absent in the F550M filter images and weak in the F330W filter. These aperture-size effects may also account for the discrepancy between previous models and the observed Goddard High Resolution Spectrograph (GHRS) spectrum of η Car (Hillier et al.

2001; Ebbets, Walborn, & Parker 1997).[20] Appendix A discusses the STIS spectra of the star, Weigelt objects, and some extended regions, along with the transmission curves of the ACS and WFPC2 filters we used. There we also discuss in more detail the contribution of reflected starlight and intrinsic nebular emission in each filter.

The possibility that UV images with *HST* can spatially resolve the outer wind of η Car is intriguing, because they may be a powerful probe of this star's unusual variability. The UV excess in the ACS images that is concentrated toward equatorial regions, if it is indeed wind emission, supports the bipolar stellar wind geometry proposed by Smith et al. (2003a).

[20] Note that the GHRS spectrum was obtained with a larger aperture ($0\rlap{.}''2 \times 0\rlap{.}''2$) than our STIS spectra ($0\rlap{.}''1 \times 0\rlap{.}''13$) and included more of the extended UV emission seen in our ACS images. Aperture-size effects in models of η Car's stellar wind will be investigated in more detail in a future paper (D. J. Hillier et al. 2004, in preparation).
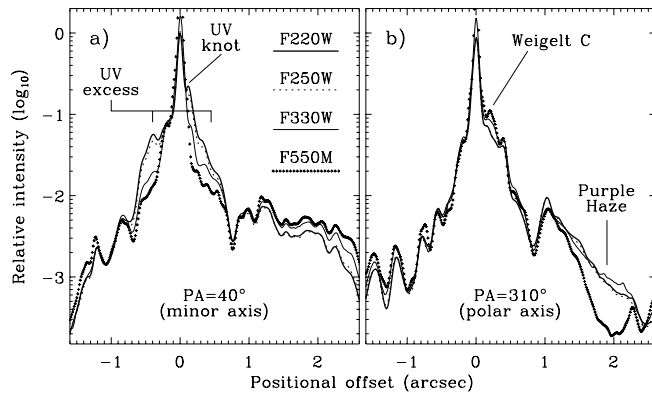
Fig. 4.—Tracings of the spatial intensity distribution in the various filter images shown in Fig. 1: F220W (*thick solid line*), F250W (*dotted line*), F330W (*thin solid line*), and F550M (*plus signs*). Each panel shows the observed intensity along a $\sim 0\rlap{.}''6$-wide aperture passing through the central star, oriented along the minor axis (P.A. = 40°) in (*a*) and roughly along the major (i.e., polar) axis at P.A. = 310° in (*b*). For each filter image, the relative intensity is normalized to an arbitrary value close to the peak of the central star. The multiplicative constants for each filter are 1.30×10^{-18} (F220W), 2.79×10^{-17} (F250W), 6.51×10^{-17} (F330W), and 1.74×10^{-17} (F550M) ergs s^{-1} cm^{-2} $\mathrm{\AA}^{-1}$ $arcsec^{-2}$.

However, the UV emission does not tell us if this wind geometry arises from intrinsic properties of a rotating central star, or to what degree the latitude dependence may be influenced by ionization from a hot companion star. Furthermore, the latitude dependence of the wind is expected to change severely during one of η Car's "spectroscopic events" (Smith et al. 2003a). Again, it is not yet known if the events are due to a shell ejection by the primary star, perhaps triggered by a close-passing companion, or instead due to ionizing photons from a hot companion star getting trapped as it plunges into the dense wind of the primary (e.g., Zanella, Wolf, & Stahl 1984; Damineli et al. 1997; Davidson 1997, 1999). If the higher ionization at low latitudes is caused by a hot companion in an eccentric orbit, then severe departures from azimuthal symmetry can be expected during an event (moving

shadows, etc.). Continued monitoring with ACS/HRC UV images during the 2003.5 event could provide a unique test.

3.3. Comparison of UV, Optical, and IR Structure

Figure 6*b* compares the relative spatial distributions of the excess UV emission and the thermal-emitting dust. Contours in Figure 6*b* show the emitting optical depth at 8.8 μm (from Smith et al. 2003b), which traces the column density of dust heated to a few hundred kelvins. These contours give the best representation of the IR dust torus, invoked by many observers (e.g., Morris et al. 1999; Smith et al. 2002). Locations to the northeast and southwest of the star where the dust column density is lowest are filled in by excess UV emission. Thus, Figure 6*b* supports the scenario advanced earlier by Smith et al. (2000, Fig. 8), that ionized equatorial gas resides interior to the dust torus, perhaps as part of a contiguous structure (see also Gull & Ishibashi 2001). A disk of this sort has been inferred independently from imaging polarimetry (Falcke et al. 1996). The boundary between the outer wind and nebular torus is not clear.

Not all emission seen in Figure 6*a* is necessarily near the equatorial plane. Limb-brightened walls of the polar lobes overlap with equatorial material, so kinematics of the gas at positions with strong emission in Figure 6*a* are of interest. Figure 7 shows position-velocity maps with STIS slits placed nearly perpendicular to the polar axis of the Homunculus at three different offset positions (Fig. 6*c*). These run through the Purple Haze (7*a*), the Weigelt objects C and D (7*b*), and the star itself (7*c*). Positions to the northwest of the star show a redshifted [N II] ring with heliocentric velocities up to 200 km s^{-1}, whereas the position through the star shows a distorted blueshifted ring in velocity space. This is expected for spatio-kinematic cross sections through the Little Homunculus at those same positions (Ishibashi et al. 2003; Smith 2002). We surmise that some of this emission may come from the receding northwest polar lobe of the Little Homunculus seen through a region of low extinction in the equatorial skirt. Indeed, the Fan appears to be a region with lower dust column density (Smith et al. 2003b).
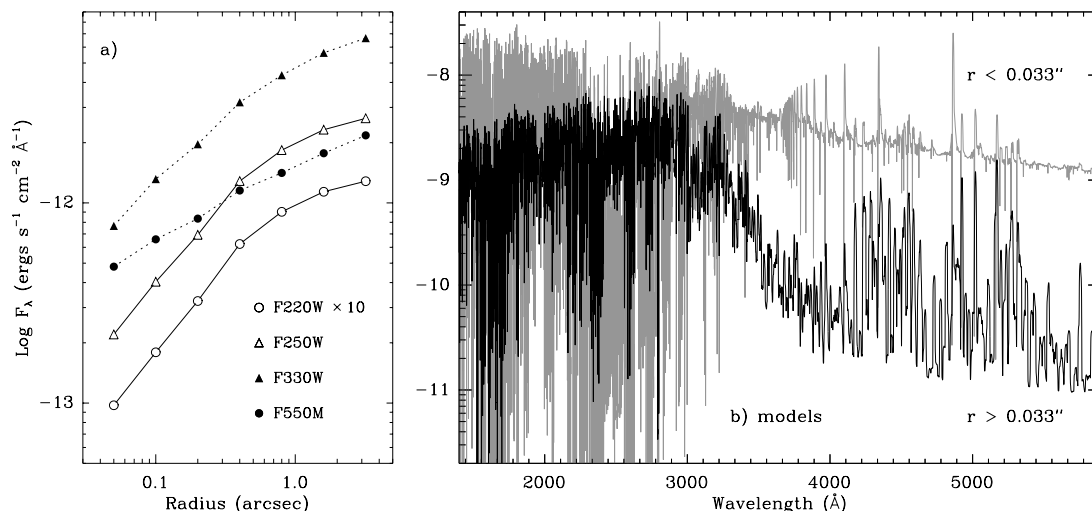
Fig. 5.—(*a*) Photometry for a range of circular aperture radii centered on the star in each of the four ACS/HRC filters. Each point represents the total encircled flux at a given radius in 2002 November. Note that data from the F220W filter have been multiplied by a factor of 10 for display here. (*b*) Radiative transfer models of the emission from η Car's wind (see Hillier et al. 2001). The gray line shows the predicted emission from the star measured in an aperture of radius $0\rlap{.}''033$, while the black line shows the rest of the wind emission originating outside that radius. Note the difference in the relative continuum level between the UV and visual. The absolute flux here is stronger than we measure from images, because the models do not include extinction from dust along the line of sight.

Fig. 6.—Various displays of the spatial distribution of emission structures in the core of the Homunculus nebula. (*a*) Flux-ratio image comparing the F220W and F550M images; dark areas d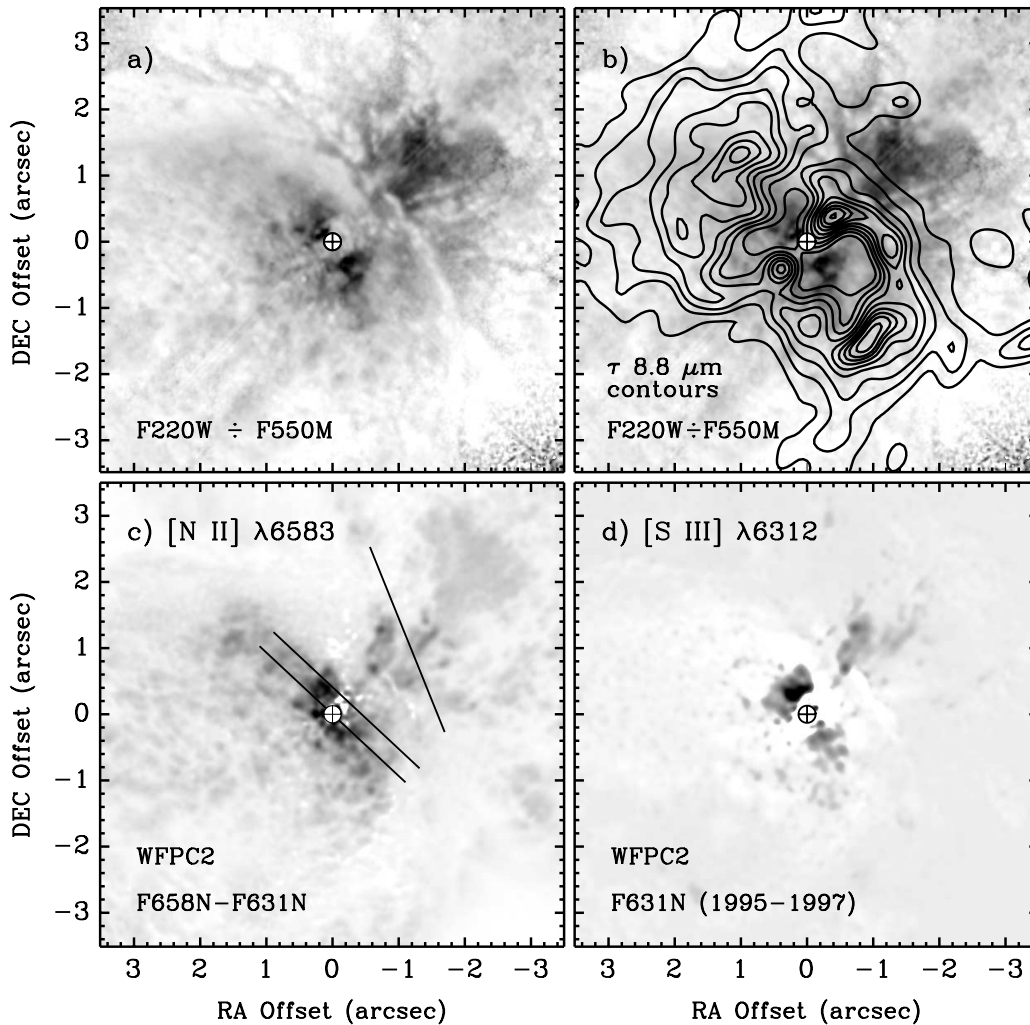enote stronger UV emission. Regions colored black are roughly a factor of 4 stronger with the UV filter. (*b*) Same as (*a*), but with contours of 8.8 μm emission optical depth superposed (from Smith et al. 2003b; individual contour levels range from a τ of 0.08 to 0.44). (*c*) Continuum-subtracted [N II] λ6583 image made from narrowband *HST* WFPC2 images (Morse et al. 1998; Smith et al. 2000). The diagonal lines show locations of the 0″1 STIS apertures used to obtain the data in Fig. 7. (*d*) Spatial distribution of temporally variable [S III] λ6312 emission features as seen in multiepoch *HST* WFPC2 images (see Smith et al. 2000).

Figures 8*a* and 8*b* show IR images of the putative dusty torus inside the Homunculus of η Car. This disrupted torus is thought to mark the position in the equatorial plane where the two hemispheres of the Homunculus meet, a few thousand AU from the star (Smith et al. 2002; Smith 2002). The main distinguishing features are a bright condensation about 1″ northeast of the star and an incomplete arc toward the southwest (the "SW Arc"; see also Rigaut & Gehring 1995). Figures 8*c* and 8*d*, on the other hand, show a much smaller field of view near the star, as seen in the new ACS/HRC images with the F220W and F550M filters. UV emission within about 0″2 of the central star has a morphology similar to the dusty IR torus, *even though it covers orders of magnitude smaller spatial scales*. This extended UV emission close to the star is elongated along roughly the same position angle as the larger IR torus, orthogonal to the polar axis of the Homunculus. Both wavelength regimes show two prominent emission peaks, one toward the northeast (NE) and one toward the southwest (SW Arc). Positional information for these two features is listed in Table 2, where we can see that the position

angles for the two groups of features are identical in the UV and IR, within the uncertainty, as are ratios of their distances from the star, $R_{\mathrm{SW\ Arc}}/R_{\mathrm{NE}}$. In other words, if the UV image were enlarged and superposed on the IR image, the NE and SW Arc features would overlap in the two wavelength regimes. The NE and SW Arc features seen in the UV are absent in the optical F550M image, but they do have counterparts in high-resolution optical speckle-polarization maps by Falcke et al. (1996), who interpreted the features as an equatorial disk. Several other knots, of which C and D are the brightest, are seen surrounding the star, presumably due to scattered light from their dusty cores. This distribution of knots in the F550M image resembles the condensations farther out in the equatorial skirt that are seen all around the star in images at $\sim$2 μm (Smith et al. 1998).

This is not the first detection of small-scale features resembling larger structures around η Car: the discovery by Ishibashi et al. (2003) of a bipolar "Little Homunculus" expanding inside the larger one rests on such a comparison (see also Walborn 1976, regarding structures in more distant
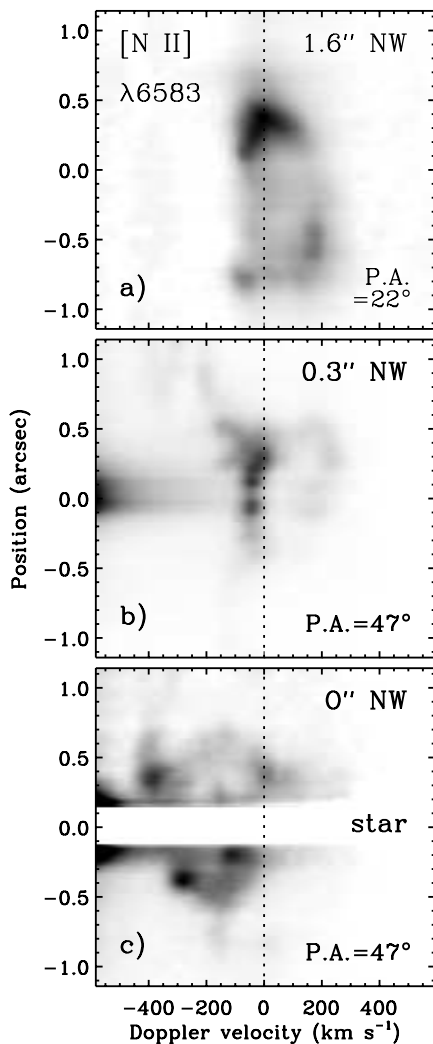
Fig. 7.—Position-velocity maps of [N ii] λ6583 through STIS long-slit apertures corresponding to the diagonal lines in Fig. 6c, crossing through (a) the Fan, (b) the Weigelt blobs, and (c) the star. Continuum emission has been suppressed, and the region close to the star in (c) has been masked-out during data processing (not by an occulting mask during observation). The spectrum in (a) was obtained on 2001 April 17, and the spectra in (b) and (c) were obtained on 1998 November 25.

ejecta). As is the case with the equatorial features discussed here, the larger bipolar Homunculus is dusty when seen in scattered light and thermal-IR emission, but the Little Homunculus is seen in emission lines at visual wavelengths. Ishibashi et al. (2003) conclude that the Little Homunculus may have been ejected in the 1890 outburst of η Car, while it is known that the larger Homunculus originated in the Great Eruption. Thus, we ask: Does the "little torus" seen in the UV correspond to the Little Homunculus in the same way that the larger IR torus corresponds to the Homunculus nebula? If the IR torus and the smaller UV feature were ejected in separate mass-loss episodes, their similar morphology would indicate longitude-dependent mass loss that has been persistent, as expected with phase-dependent mass loss in a close-binary system (e.g., Corcoran et al. 2001; Duncan & White 2003; Monnier, Tuthill, & Danchi 2002; Williams et al. 1990; Tuthill, Monnier, & Danchi 1999).

4. KINEMATICS OF THE WEIGELT OBJECTS

The bright core of the inner Homunculus contains several compact ($\sim0\farcs05$) nebular condensations (i.e., "knots" or

"blobs"; see Fig. 2d). The brightest of these (objects B, C, and D) were first spatially resolved from the central star (object A) by Weigelt & Ebersberger (1986) and Hofmann & Weigelt (1988) and are generally called the "Weigelt objects." They are nebular condensations that emit blueshifted narrow-line spectra different from the broad-line spectrum of object A (see Appendix A and Davidson et al. 1995, 1997). Comparing positions first measured in 1985 using speckle interferometry with pre-COSTAR *HST* images of η Car obtained in 1992, Weigelt et al. (1995) concluded that B, C, and D were significantly younger than the rest of the Homunculus. However, these two data sets were obtained through different filters (8500 and 5500 Å), and the pre-COSTAR images suffered from spherical aberration. During the past decade, a more consistent set of images have been obtained with WFPC2 and ACS, which we use to reassess the age of these features.

Measuring their motion is not trivial, since their positions, sizes, and shapes vary depending on the wavelength observed, and their shapes change with time in multiepoch WFPC2 images. Below we employ three different and independent measurement techniques: (1) one-dimensional intensity tracings through the star and each of the condensations, (2) two-dimensional radial profile fits, and (3) flux-weighted centroids. The one-dimensional tracings are especially interesting, as they clearly illustrate some of the pitfalls associated with measurements of this sort, particularly with regard to certain filters contaminated by nebular emission lines. We focus our analysis on the speckle objects C and D; object B is too near the star to give reliable results over the short time baseline.

4.1. *The Central Star*

Using processed *HST* images made with the *HST* Faint Object Camera (FOC), WFPC2/PC, and ACS/HRC instruments, we made one-dimensional tracings of the spatial intensity distribution crossing through the central star and each of the two objects C and D. First, the pixel scales of all images were subsampled to match our reduced ACS/HRC images ($0\farcs0125$), and then rotated so that a given position angle fell on a constant row of pixels (P.A. = 300° for C, and P.A. = 336° for D). We extracted a segment 4 pixels wide ($0\farcs05$) through the star, and C or D. Before discussing C and D, we first evaluate the profiles of the central star.

Figure 9 shows intensity tracings through the central star at both position angles for three different WFPC2 filters and the F550M filter of the FOC and ACS/HRC. Figure 9 allows us to evaluate the extent to which telescope focus or spacecraft jitter may affect the spatial resolution. Ignoring the pre-COSTAR F550M FOC profile (which suffers from uncorrected spherical aberration), the F550M (ACS), F631N, and F658N filters give remarkably consistent results, with typical FWHM values of $0\farcs05$, $0\farcs055$, and $0\farcs06$, respectively. The profiles for the F336W filter, however, are less reassuring, with variable profile shapes and FWHM values that vary between $0\farcs065$ and $0\farcs08$. One exception seems to be the WFPC2 observation in 1999 June (Fig. 9, *thin solid line*). In the otherwise well-behaved F631N filter, for example, the FWHM for 1999 June is $\sim0\farcs08$, compared to the usual $0\farcs055$ at other epochs. It is suspicious that the FWHM is significantly larger only in 1999 June, a little more than 1 yr after a spectroscopic event in which a shell ejection may have taken place. Future work is needed to explore the multiwavelength and multiepoch behavior of the star in more detail, but for now, one might choose to interpret the 1999 June measurements of the Weigelt objects with some caution.
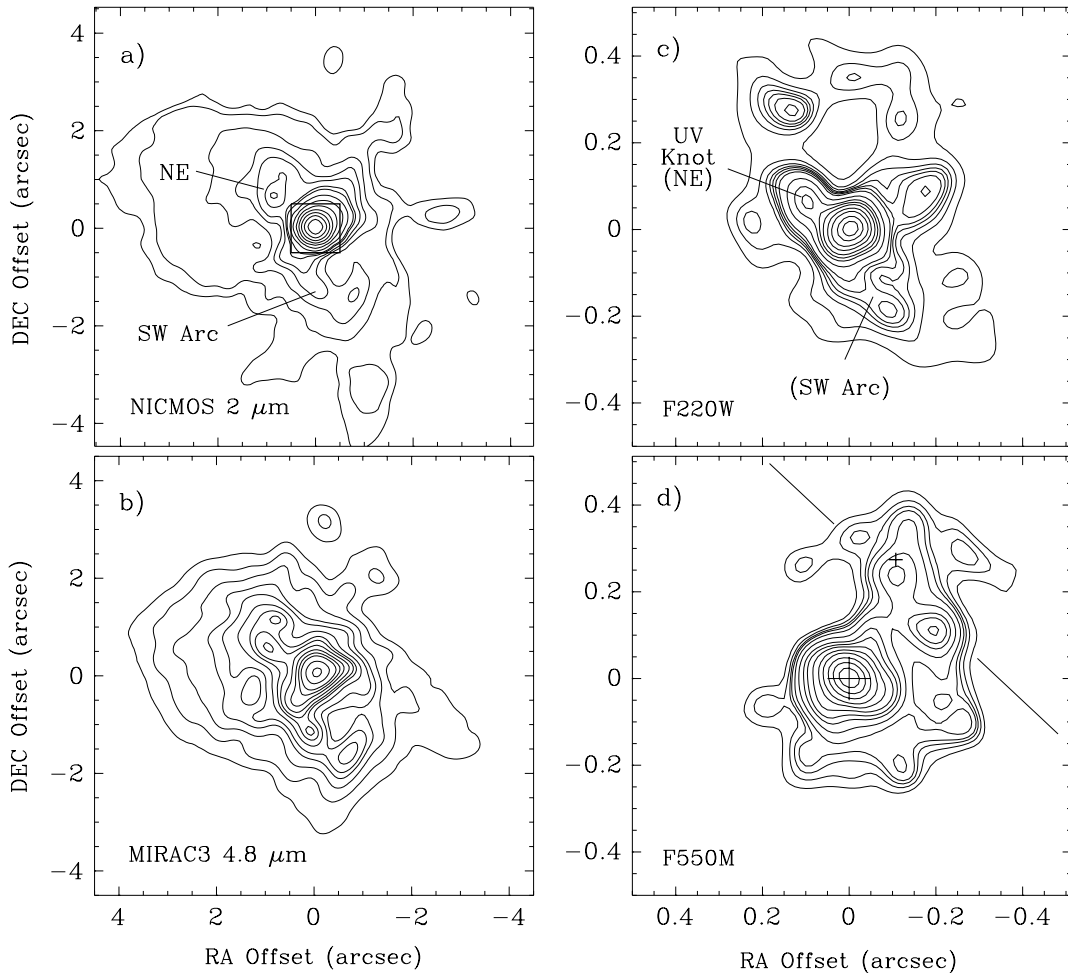
Fig. 8.—Comparison of previously recognized IR dust structures in the core of the Homunculus (*left panels*) with compact features near the star seen in the new ACS/HRC images (*right panels*). Note the very different size scales between the left and right panels in this figure. (*a*) Near-IR scattered light in the 2.15 μm continuum filter, obtained with *HST* NICMOS (Smith & Gehrz 2000). The small box around the star shows the field of view in (*c*) and (*d*). (*b*) Thermal emission from hot dust at 4.8 μm, observed with the MIRAC3 camera at the Magellan Observatory (Smith et al. 2003b). (*c*) Inner 1″ region around the star seen by ACS/HRC through the F220W filter. (*d*) Same as (*c*), but using the F550M filter. The diagonal line shows the position and orientation of the 0″.1-wide STIS slit aperture used to measure the radial velocities of the Weigelt objects (see § 4.6). The small cross marks the position of D measured by Dorland et al. (2004), relevant to the discussion of its proper motion in Appendix B. Contour levels for (*a*) and (*b*) can be found in Smith & Gehrz (2000) and Smith et al. (2003b), respectively. Contours in units of 10^{-13} ergs s^{-1} cm^{-2} Å^{-1} arcsec^{-2} are 0.9, 1.2, 1.4, 1.6, 1.7, 1.8, 2, 2.5, 3.5, 4.5, 5.5, 7, 9.5, 13.5, and 18.5 for the F220W image in (*c*), and 8.5, 11, 13.5, 16, 20, 25, 35, 45, 55, 75, 115, 230, 460, and 920 for the F550M image in (*d*). The features labeled in (*a*) and (*c*) correspond to the discussion in § 3.3.

4.2. *One-Dimensional Tracings of the Weigelt Objects*

Figure 10 shows spatial intensity tracings through C and D with the F336W, F631N, and F658N filters of WFPC2, and F550M tracings for the FOC and ACS data. After studying Figure 10, one conclusion we draw is that the F336W and F658N filters are not reliable indicators of the motions of the Weigelt objects, probably because of severe contamination by time-variable and spatially dependent nebular emission lines (see Appendix A). Their profile shapes change significantly in these filter images, and they exhibit irregular "motion." Thus, any proper-motion measurement for these condensations that relies on the F336W or F658N filters would be dubious. In general, C seems to be more well behaved than D, with "well-behaved," meaning incremental, outward motion.

The F631N and F550M filter images, on the other hand, appear more reliable, and the two different filters give consistent results. Both are dominated by reflected continuum light (see Appendix A), with the exception of some [S III] λ6312 captured within the F631N bandpass during high-

excitation phases of η Car's 5.5 yr cycle. The only severe change in profile shape in the F631N filter images is a broadening on the outer edge of object D in 2001, at the peak of the high-excitation phase, which is also seen in the F658N filter images at the same epoch.[21] Thus, if we regard high-excitation phases with some caution, the F550M and F631N images are useful indicators of the positions of the Weigelt objects. It is likely that reflected visual continuum gives the most reliable estimate of the objects' positions, since dust should survive in the dense cores of these objects more readily than in their ionized outer layers (see § 4.6). Compared to the F336W and F658N images, the condensations are even more fuzzy and their positions more ill-defined in the ACS/HRC UV images (Fig. 4*b*).

------

[21] In 1999 June we see no systematic broadening of the spatial profile for object C or D that would be consistent with relatively poor spatial resolution in this epoch. Therefore, the broad spatial profile of the star in this epoch may be real.

Parameter	UV	IR
PA$_{NE}$ (deg)	56	54
PA$_{SW\ Arc}$ (deg)..	205	206
R$_{NE}$ (arcsec)	0.12	1.1
R$_{SW\ Arc}$ (arcsec)...	0.20	1.7
R$_{SW\ Arc}$/R$_{NE}$..	1.7	1.6

NOTE.—The uncertainty in the position angles is roughly ±5°, and the uncertainty in the separation from the star is about ±5%.

Table 3 lists the positions for C and D along constant position angles of 300° and 336°, respectively. We determined these positions by measuring the center between the inner and outer profile wings at 90% of the emission peak for each object at each epoch. One exception was C in 1992, for which

spherical aberration of the star's PSF filled in the space between the condensation and the star up to almost 90%, so in this isolated case we measured the center at 93% of the peak.

4.3. Two-Dimensional Radial Profile Fits

Based on the results of § 4.2, we restrict further discussion of the Weigelt objects' motion to the F631N and F550M filter images. To check the positions derived by the method described above, we also measured the positions of C and D in deconvolved but unrotated images using a two-dimensional Gaussian radial profile fit, with radii between 0″05 and 0″07. From these measurements, we derived separations and position angles at each epoch, as listed in Table 3. Small but significant changes in position angle, combined with small differences compared to the technique described above indicate that the blobs change shape with time and are partially resolved with irregular shapes. Visual inspection of the images
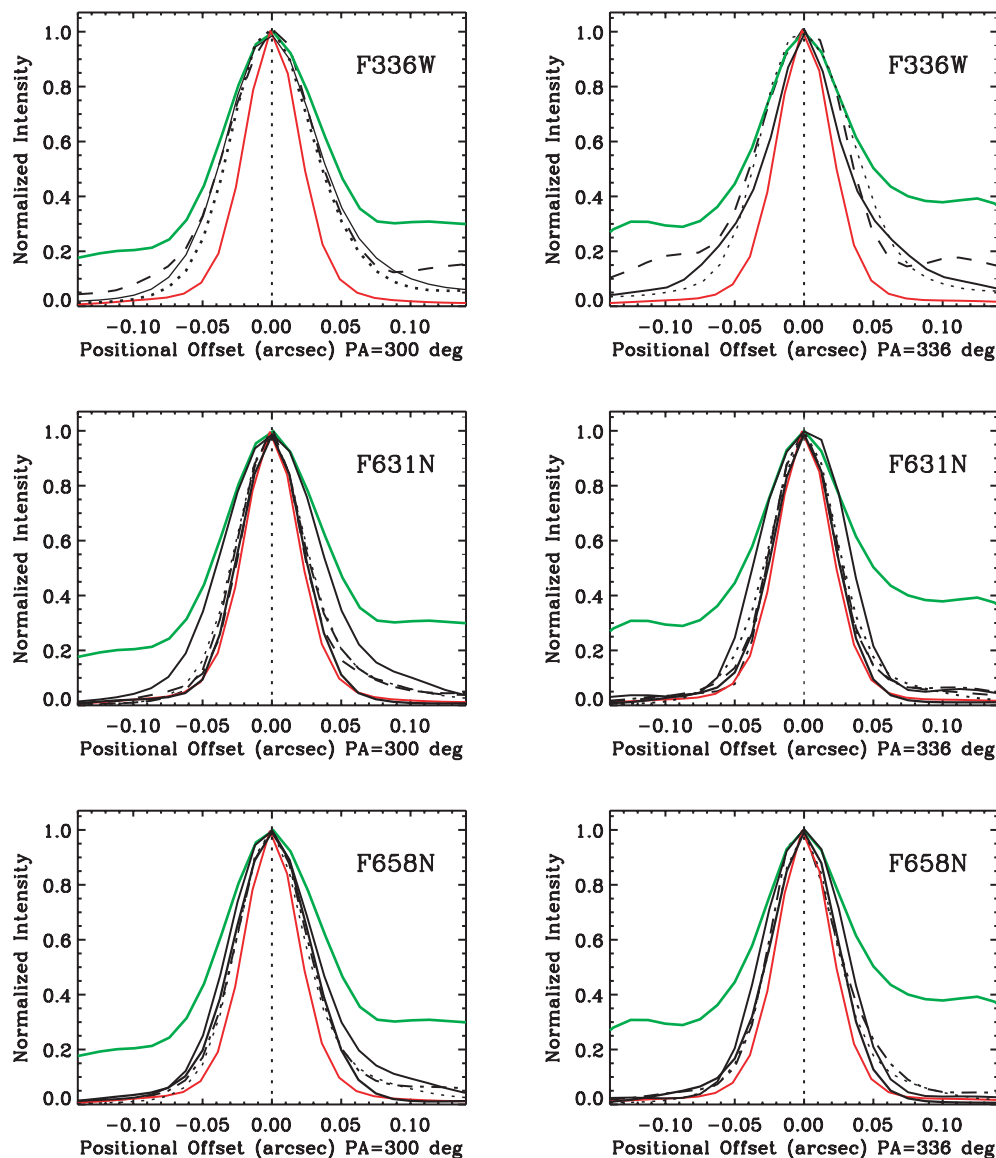

FIG. 9.—Normalized intensity tracings through images of the star at P.A. = 300° (*left panels*; corresponding to tracings of object C in Fig. 10) and P.A. = 336° (*right panels*; corresponding to object D) for the indicated WFPC2 filters. The same line style is used to plot each epoch in each panel: 1995 (*dot-dashed line*), 1997 (*dashed line*), 1999 (*thin solid black line*), 2001 (*dotted line*), and 2003 (*thick solid line*). In each panel, we also show F550M filter images obtained with the FOC in 1992 (*green*) and with the ACS/HRC in 2002 (*red*). Intensity tracings were made with a synthetic aperture 0″05 wide on rotated FOC, WFPC2, and ACS images, all matched to the same pixel scale of 0″0125.
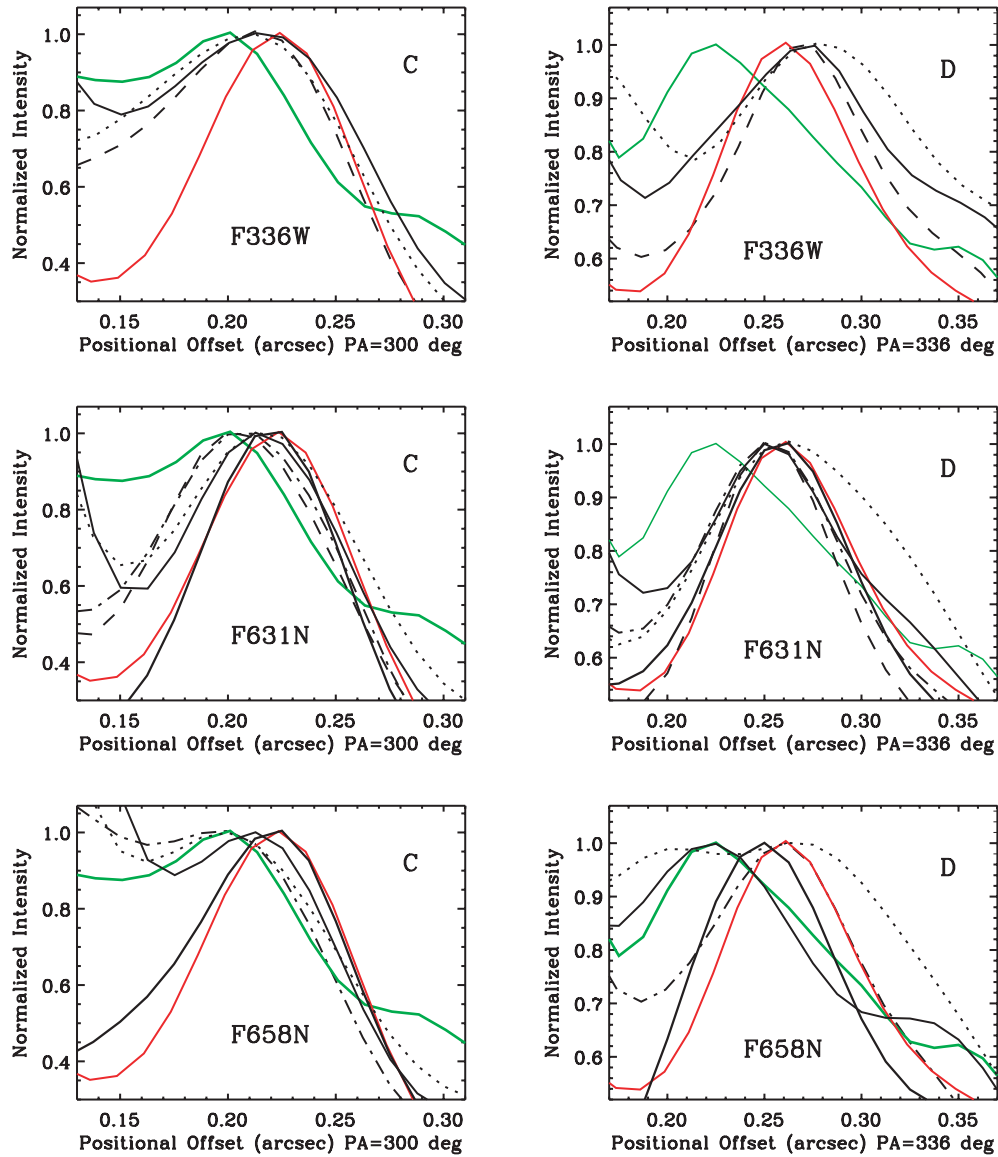
Fig. 10.—Normalized intensity tracings through the Weigelt objects C, at P.A. = 300° (*left panels*), and D, at P.A. = 336° (*right panels*), for the indicated WFPC2 filters. The plotted position is relative to the central star. The same line style is used to plot each epoch in each panel: 1995 (*dot-dashed line*), 1997 (*dashed line*), 1999 (*thin solid black line*), 2001 (*dotted line*), and 2003 (*thick solid line*). In each panel, we also show F550M filter images obtained with the FOC in 1992 (*green*) and with the ACS/HRC in 2002 (*red*). Intensity tracings were made with a synthetic aperture 0″.05 wide on rotated FOC, WFPC2, and ACS images all matched to the same pixel scale of 0″.0125.

creates a similar impression. In other words, we should expect different measurement techniques to give slightly different results.

4.4. *Flux-Weighted Centroids*

Finally, we employed a third independent measurement technique to estimate the positions of the Weigelt objects. We used the flux-weighted centroid algorithm of the PHOT task in IRAF's DIGIPHOT package to estimate the position of objects C and D relative to the star at each epoch in deconvolved but unrotated *HST* images. The resulting separations between the blobs and the star, along with the corresponding position angles, are listed in Table 3.

4.5. *Analysis of the Proper-Motion Measurements*

Measurements (shown in Table 3) using the three different methods described above are plotted in Figure 11 along with

the first speckle measurements by Hofmann & Weigelt (1988). Circles correspond to the one-dimensional tracings, diamonds to the two-dimensional radial profile fits, and asterisks to the flux-weighted centroid measurements. Error bars plotted for the circles apply to other plotted symbols as well, and the sizes of the error bars (6.2 mas) represent the average of the 2 σ deviation of the three different measurement methods for each epoch. We plot 2 σ error bars to account for 1 σ uncertainty in measuring both the position of each condensation and the central star. (Note, however, that we show larger error bars for pre-COSTAR images.)

Figure 11 leaves little doubt that the Weigelt blobs are indeed moving away from the star. Unweighted, least-squares fits to all the *HST* data in Figure 11 (*solid line*) give ejection dates of 1909 and 1907 for objects C and D, respectively. Uncertainty in each derived ejection date is about ±12 yr. Note that this fit *excludes* the first measurement by Hofmann &

TABLE 3
Positions of the Weigelt Objects C and D Relative to η Car

Parameter	1992.841	1995.721	1997.436	1999.447	2001.425	2002.786	2003.119
Filter.........................	F550M	F631N	F631N	F631N	F631N	F550M	F631N
Instrument	FOC	WFPC2	WFPC2	WFPC2	WFPC2	ACS	WFPC2
C pos., rad. (arcsec)...............	0.199	0.208	0.210	0.217	0.217	0.221	0.218
C P.A. (deg)..........................	304.0	297.6	299.4	301.4	300.6	299.9	303.1
D pos., rad. (arcsec)...............	0.235	0.242	0.250	0.252	0.256	0.261	0.256
D P.A. (deg)..........................	336.0	335.9	336.3	337.8	331.5	334.3	334.6
C pos., 1D-300 (arcsec).........	0.199	0.207	0.205	0.215	0.217	0.223	0.220
D pos., 1D-336 (arcsec)	0.227	0.252	0.253	0.254	0.264	0.261	0.259
C pos., cent. (arcsec)	0.195	0.201	0.204	0.204	0.217	0.224	0.223
C pos., med. (arcsec).............	0.202	0.204	0.206	0.205	0.222	0.225	0.224
C P.A. (deg)..........................	303.2	300.9	301.2	303.5	301.2	299.1	302.5
D pos., cent. (arcsec).............	0.224	0.247	0.252	0.246	0.264	0.259	0.257
D pos., med. (arcsec).............	0.230	0.252	0.257	0.249	0.272	0.263	0.261
D P.A. (deg)..........................	359.7	336.0	335.8	337.9	335.6	335.4	335.6

Note.—Separations and position angles for C and D were measured using two-dimensional Gaussian radial profile fits (rad.), one-dimensional intensity tracings (1D-300 or 1D-336) along P.A. = 300° and 336°, respectively, as described in the text (also see Fig. 11), or a flux-weighted centroid without (cent.) and with (med.) median filtering applied.

Weigelt, made at a very different wavelength (8500 Å), even though this initial measurement agrees well with the fit to the *HST* data. A fit including these initial ground-based measurements changes the derived ejection dates only slightly (Fig. 11, *dashed lines*). Thus, we adopt an average ejection date of 1908 ±12 yr for objects C and D. The historical light curve of η Car shows no "event" occurring shortly after 1900 (e.g., Humphreys et al. 1999). Here we investigate whether the Weigelt blobs could have been ejected during the smaller outburst of η Car seen around 1890 and then accelerated during the past century (see also Davidson et al. 1997). A change in the apparent ejection date of less than 10 yr, or about 10% of the age, is needed to be consistent with the
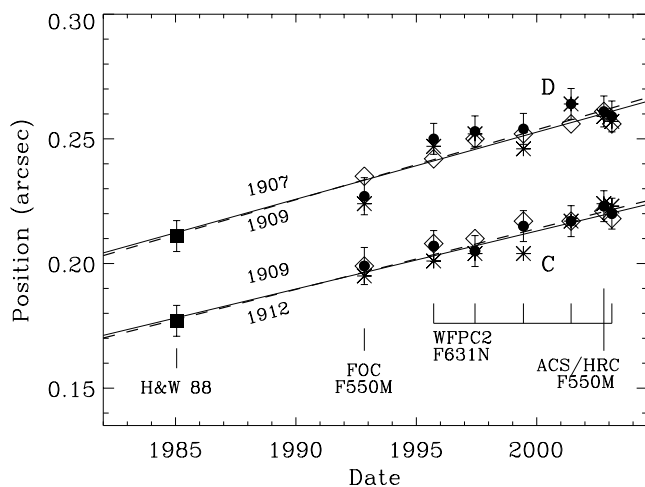

Fig. 11.—Proper motion of the Weigelt objects C and D. Positions measured in our new ACS/HRC images with the F550M filter are combined with positions measured in WFPC2 images through the F631N filter, as well as pre-COSTAR *HST* FOC images taken in 1992 through the F550M filter and the early speckle images made by Hofmann & Weigelt (1988) in 1985 (*squares*). The dashed lines show least-squares fits to all data points, and the solid lines show least-squares fits that include only *HST* data. Circles for *HST* data are from one-dimensional tracings, diamonds are measured with two-dimensional Gaussian radial profile fits, and asterisks are from a flux-weighted centroid. Positions measured with a flux-weighted centroid on median-subtracted images (see Table 3) are not shown and are not included in the fits (see Appendix B).

uncertainty in our measurements. This would require a velocity increase Δv of less than 10 km s^{-1}, if the blobs are now moving away from the star with a speed of order $\sim$40 km s^{-1} (including a correction for the projection angle of 42° out of the plane of the sky; Smith 2002; Davidson et al. 2001).

With η Car's luminosity of $L \approx 5 \times 10^6\ L_\odot$ and a huge mass-loss rate of $\sim$10$^{-3}\ M_\odot$ yr^{-1} (Hillier et al. 2001), both radiation pressure and ram pressure from the stellar wind might significantly affect the motion of a gas condensation located at a distance of only $R \approx 1.2 \times 10^{16}$ cm ($\sim$800 AU) from the central star (the distance of object D, for example). The wind's ram pressure may exceed radiation pressure in the polar wind (Smith et al. 2003a) but is latitude-dependent and difficult to quantify. Therefore, let us make a conservative plausibility argument based only on the force of radiation, keeping in mind that the wind's ram pressure will add to the expected acceleration. If we make the simplifying assumptions that a blob is optically thick and its radius r increases in proportion to its distance R from the star (its solid angle seen by the star is constant), then the expected change in velocity at time t is of order

$$\Delta v \approx \frac{L}{4mc}\left(\frac{r}{R}\right)^2 t,$$

where m is the mass of a single condensation and the luminosity is assumed to be constant during this time. A plausible value of m is 0.01 $M_\odot$ (Smith et al. 2003b; Hamann et al. 1994; Davidson et al. 1995), while our ACS data indicates that $0.11 < r/R < 0.17$. With these parameters, the radiation-pressure effect for 110 yr turns out to be $\Delta v \approx$ 3–8 km s^{-1}. The total acceleration will be larger if backscattering and the stellar wind's ram pressure are included in the estimate. Thus, with favorable assumed values and with the stated uncertainties in the derived ejection date, the expected acceleration is large enough that an origin for the Weigelt objects during the 1890 outburst is plausible. However, based on available data we cannot yet exclude the possibility that they may have been ejected after 1890.[22]

---

[22] Dorland, Currie, & Hajian (2004) have recently presented independent measurements of the Weigelt objects and find a younger age than we do, with ejection dates closer to 1940. Appendix B discusses detailed differences between their measurements and ours and partially accounts for the discrepancy.

The Weigelt objects probably reside near η Car's equatorial plane (see § 4.6), and an $\sim$1890 ejection date is related to the question of the age of the large-scale equatorial skirt of the Homunculus. Several authors have cited evidence that some features in the ragged equatorial debris may have been ejected after the Great Eruption, in the 1890 outburst (Gaviola 1950; Ringuelet 1958; Gehrz & Ney 1972; Duschl et al. 1995; Weigelt et al. 1995; Davidson et al. 1997, 2001; Davidson & Humphreys 1997; Smith & Gehrz 1998). However, Morse et al. (2001) used *HST* WFPC2 images to measure proper motions and concluded that the most prominent features in the equatorial debris outside a radius of $\sim$2″ from the central source originated in the Great Eruption. Various clues, including multiple radial-velocity components, indicate that material from *both* outbursts can be seen in the equatorial ejecta near the star. Material from the Great Eruption dominates the appearance of high-resolution *HST* images that trace continuum emission, while material from the 1890 eruption is seen primarily in Doppler-shifted nebular-emission lines (Davidson et al. 2001; Smith 2002).

4.6. Radial Velocities and Projection Angles

From the fits in Figure 11, we measure proper motions of $\dot{\theta}_C = 2.34 \pm 0.3$ mas yr^{-1} and $\dot{\theta}_D = 2.70 \pm 0.3$ mas yr^{-1}. Here we augment these proper motions with observed Doppler shifts to investigate the location of the Weigelt objects relative to the central star. Emission lines in the Weigelt objects have been observed with *HST* STIS on several separate occasions, but at one particular epoch, on 1998 November 25, the slit aperture was positioned to include both Weigelt objects C and D at the same time (see Fig. 8d). The spectral resolution $R = \lambda/\Delta\lambda$ was 5000–10,000. These observations had limited wavelength coverage, sampling a few different parts of the spectrum from the UV to red wavelengths, but enough of the narrow emission lines were recorded to be useful in our analysis here. We selected several lines throughout the spectrum, using only isolated lines that are free of blends. Table 4 lists the observed wavelengths and heliocentric velocities for several lines in both C and D; these values are the average of a flux-weighted centroid and a Gaussian fit to the line profile. Vacuum wavelengths are taken from Zethson (2001).

From UV emission lines, Davidson et al. (1997) measured a combined heliocentric velocity for the Weigelt objects of about -47 km s^{-1}. After correcting this value for a likely

systemic velocity for η Car of -7 km s^{-1} and combining it with proper-motion estimates available at the time, they concluded that the Weigelt objects were in equatorial zones of η Car's ejecta, where the assumed inclination angle of the Homunculus at that time was $i = 35°$ (more recent studies indicate $i \approx 42°$; see below). Our new ACS images at UV wavelengths give some pause, however, because the blobs appear more amorphous and diffuse, with positions less well defined than at visual wavelengths. As the UV images are not the best indicators of proper motion for these emission-line blobs, so too the UV emission lines may not be the best tracers of the blobs' actual Doppler velocities. One possible scenario is sketched below:

The Weigelt objects are dense condensations moving away from the star at only $\sim$10% of the speed of the stellar wind that engulfs them; the analogy of a comet is not wholly inappropriate. Suppose that a dense, almost stationary "neutral"[23] globule is bathed in a strong UV radiation field and pounded by a less-dense stellar wind moving past the globule at several hundred km s^{-1}. As material is photoionized and photoevaporated from the globule's surface layers, it will be ablated by radiation pressure or ram pressure from the wind (see § 4.5). This material may form an ionized "coma" around the globule, and may then have some net motion toward us relative to the globule's core, initially at speeds near the sound speed. This anomalous motion would be traced by lines such as Fe II (pumped by Lyα), [Ne III], He I, [Fe III], [S III], and other lines that are seen to vary during η Car's 5.5 yr spectroscopic cycle (see Damineli et al. 1998). Thus, if such a scenario were important we should expect these high-excitation lines to have a velocity shift of order -10 km s^{-1} compared to low-ionization and low-excitation metal lines that emit from the globule's core.

This appears to be the case. The first three lines in Table 4 give average heliocentric velocities of $v_C = -47.3 \pm 1.4$ and $v_D = -48.2 \pm 2.9$ km s^{-1}, indicative of high-ionization lines such as [Ne III] and high-excitation lines such as Fe II pumped by Lyα. These measurements are consistent with the value of -47 km s^{-1} given by Davidson et al. (1997), based on the

---

[23] Here we use "neutral" to describe the region where hydrogen is predominantly H I, while other species such as Fe are still singly ionized. Moving outward, there is an important transition region where H II and Fe II coexist, before iron becomes Fe III (see Verner et al. 2002; Johansson & Letokhov 2001). This transition region is where Lyα-pumped Fe II lines may form.

TABLE 4
Heliocentric Radial Velocities of the Weigelt Objects

λ_{vacuum} (Å)	ID	$\lambda_{obs, C}$ (Å)	$\lambda_{obs, D}$ (Å)	v_C (km s^{-1})	v_D (km s^{-1})
2507.55	Fe II	2507.15	2507.14	-47.8	-49.1
2509.10	Fe II	2508.72	2508.73	-45.4	-44.2
3869.85	[Ne III]	3869.22	3869.19	-48.8	-51.2
3939.41	Fe II	3938.88	3938.86	-40.4	-41.9
3994.19	[Ni II]	3993.65	3993.64	-40.5	-41.3
4948.75	[Fe II]	4948.08	4948.11	-40.6	-38.8
4952.12	[Fe II]	4951.43	4951.46	-41.8	-39.9
4974.78	[Fe II]	4974.09	4974.13	-41.6	-39.2
6517.88	[Fe II]	6517.03	6517.03	-39.1	-39.1
6668.64	[Ni II]	6667.74	6667.72	-40.5	-41.4
6811.10	[Fe II]	6810.20	6810.19	-39.6	-40.1
6815.45	[Ni II]	6814.59	6814.55	-37.9	-39.6

Note.—Measured from the *HST* STIS spectra of objects C and D obtained on 1998 November 25.

same Lyα-pumped Fe II and other UV lines. The remaining lines in Table 4, however, are all low-excitation and low-ionization metal lines at visual/red wavelengths with high critical densities that we might expect to emit from the neutral core of a globule, *and they give substantially different average velocities* of $v_C = -40.2 \pm 1.2$ *and* $v_D = -40.1 \pm 1.1$ km s^{-1}.[24] Based on the discussion above, we conclude that these low-excitation lines are probably better tracers of the Weigelt objects' radial velocities. (At the very least, their radial velocities are more complex than previously thought, requiring further investigation.)

Adopting $v_r \approx -33$ km s^{-1} (i.e., correcting for the same -7 km s^{-1} systemic velocity as did Davidson et al. 1997), we can combine this with a tangential velocity v_t from our estimates of the proper motion mentioned above to infer the geometry of the Weigelt objects—i.e., the projected angles of their trajectories ψ_C and ψ_D out of the plane of the sky (defined such that a condensation moving directly toward us has $\psi = 90°$). We have

$$\tan \psi = \frac{v_r}{v_t} = 209.3 \frac{v_r}{\dot{\theta} D_{pc}},$$

where $\dot{\theta}$ is the proper motion measured in mas yr^{-1}, and $D_{pc} = 2300$ pc. From the proper motions and Doppler velocities given here we find $\psi_C \approx 52°$ and $\psi_D \approx 48°$, with an uncertainty of about $\pm 10°$, dominated by the adopted systemic velocity (see Davidson et al. 1997). With an inclination angle of $i \approx 42°$ for the Homunculus (Smith 2002; Davidson et al. 2001; here i is defined like a binary system, where $i = 0°$ if the polar axis is pointed directly at us), these measurements are consistent with the notion that the Weigelt objects are in equatorial zones around η Car—although they may not be exactly in the equatorial midplane. This should not be alarming, however, because it is precluded by available observations anyway, if they have the same age. Consider the fact that the three objects B, C, and D are found at different distances from the star, and in particular, that B and D are found at roughly the same position angle relative to η Car. We have shown here that C and D have *the same heliocentric velocity despite different separations from the star*, and additional STIS data show this to be true for B (Zethson 2001; Verner et al. 2002). Thus, all three cannot be both coeval and coplanar. Either B, C, and D were ejected from the star at different times with similar speeds, or they follow trajectories with substantially different values of ψ and then cannot all be in the equatorial plane.

5. SUMMARY AND CONCLUSIONS

We have presented the first UV and optical images of η Car obtained with the ACS/HRC instrument on board *HST*. These have somewhat higher spatial resolution than previous WFPC2 images and reveal the UV morphology in the core of the Homunculus for the first time. Several main conclusions follow:

1. High-resolution images with the ACS/HRC instrument show extended UV emission along the minor axis of the nebula at 0″.1–0″.6 from the star that is absent at visual wavelengths. This excess UV emission comes from low-latitude parts of the ionized outer wind. The excess UV emission at low latitudes

appears to support a model for nonspherical geometry in η Car's stellar wind, proposed by Smith et al. (2003a).

2. At UV wavelengths, the unresolved central star contributes a smaller fraction of the total flux than at visual wavelengths. The excess UV emission at large radii is mostly due to line scattering in the outer parts of the low-latitude wind. WFPC2 images in narrow filters that include [N II] and [S III] lines show similar extended structure and indicate the presence of nebular material at the same locations.

3. Excess UV emission appears to fill the interior cavity of the larger dust torus seen previously in IR images; UV and IR emission may be separate components in a larger coherent equatorial structure.

4. The Purple Haze seen previously in WFPC2 images is also prominent in the new UV images with ACS/HRC. Emission from this region is probably a combination of diffuse line emission from the "Little Homunculus" and filaments in the equatorial skirt.

5. Within 0″.2 of the star, an equatorial structure is seen in the UV that qualitatively resembles the IR dust torus seen on size scales a factor of almost 10 larger. Together, this little UV torus and the Little Homunculus seen previously may be younger and smaller counterparts of the bipolar lobes and equatorial skirt of the larger Homunculus nebula.

6. Visual-wavelength images with ACS/HRC, primarily with the F550M filter, show several compact knots distributed in a ring within 0″.3 (700 AU) around the central star. Some of these are known as the "Weigelt objects." This confirms features seen previously in red *HST* WFPC2 images.

7. We combine the new ACS/HRC images with *HST* WFPC2, *HST* FOC, and ground-based speckle measurements to reevaluate the proper motion and age of the Weigelt objects C and D. We use three independent measurement techniques and find $\dot{\theta}_C = 2.34 \pm 0.3$ and $\dot{\theta}_D = 2.70 \pm 0.3$ mas yr^{-1}, indicating a likely ejection date (assuming linear motion) of 1908 ± 12 yr. However, we also speculate that radiative acceleration may have been important, and the actual ejection date may have been somewhat earlier—perhaps during the 1890 outburst of the star.

8. From STIS spectra, we measure a heliocentric velocity of -40 ± 1.2 km s^{-1} for both C and D, as indicated by low-ionization optical lines probably formed in their cores. This estimate differs substantially from estimates of lines in the UV that may trace loosely bound outer layers of the condensations. Correcting this new heliocentric velocity for a systemic velocity of -7 km s^{-1}, we adopt a Doppler shift of -33 km s^{-1} with respect to the star. Combined with our proper-motion estimates, we confirm that C and D are in equatorial zones of η Car's ejecta, although not necessarily located exactly in the equatorial midplane.

---

[24] Verner et al. (2002) note that the average heliocentric velocity for B and D in the STIS data, including both UV and visual-wavelength lines regardless of excitation, is -44 ± 4 km s^{-1}, intermediate between the two different values we note here.
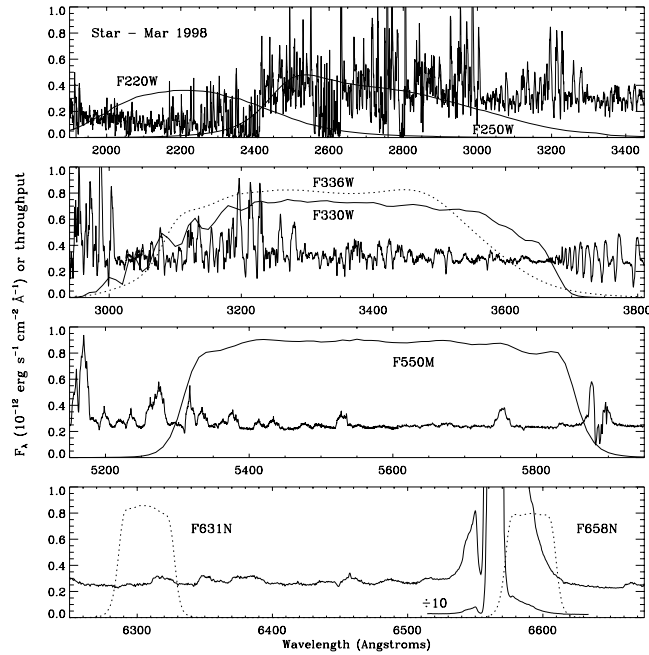
Fig. 12.—System throughput for each of the *HST* imaging filters compared with the *HST* STIS spectrum of the central star obtained in 1998 March when η Car was in the low-excitation state, just after a spectroscopic event. Solid curves are for ACS (and FOC) filters, and dotted curves are for WFPC2 filters. Filter throughput is plotted on a scale of 0–1 (for the spectrum of the star, multiply by 1×10^{-12} ergs s^{-1} cm^{-2} Å^{-1}).

APPENDIX A

CONTRIBUTIONS OF EMISSION LINES TO THE IMAGING FILTERS

The central star has a complex emission-line spectrum, and the surrounding Homunculus exhibits a mix of reflected starlight and nebular emission that varies with position and time. This complicates any analysis of multiwavelength and multiepoch images. Here we discuss various emission features that contaminate *HST* imaging filters, and we evaluate the relative contributions of intrinsic nebular lines compared to reflected lines and continuum from the star. We consider the spectrum of the central star, the Weigelt objects, and a few positions in the nebula.
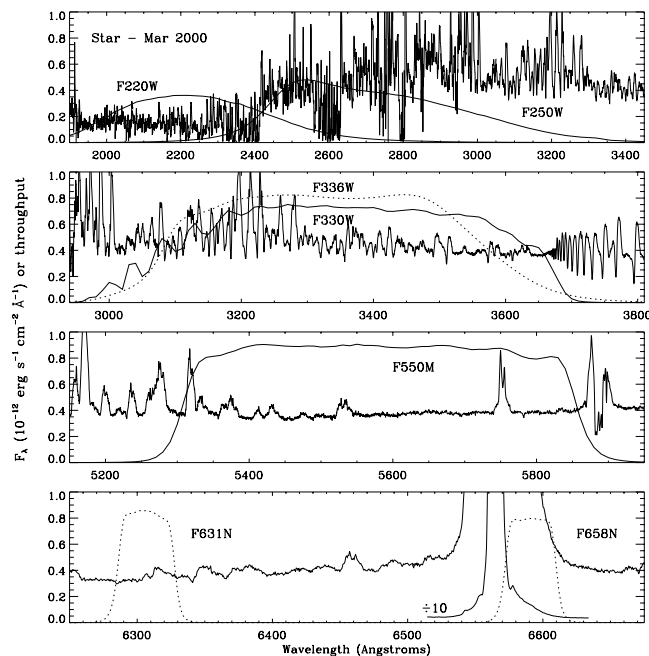
Fig. 13.—System throughput for each of the *HST* imaging filters compared with the *HST* STIS spectrum of the central star obtained in 2000 March when η Car was in the high-excitation state between spectroscopic events. Solid curves are for ACS (and FOC) filters, and dotted curves are for WFPC2 filters. Filter throughput is plotted on a scale of 0–1 (for the spectrum of the star multiply by 1×10^{-12} ergs s^{-1} cm^{-2} Å^{-1}).
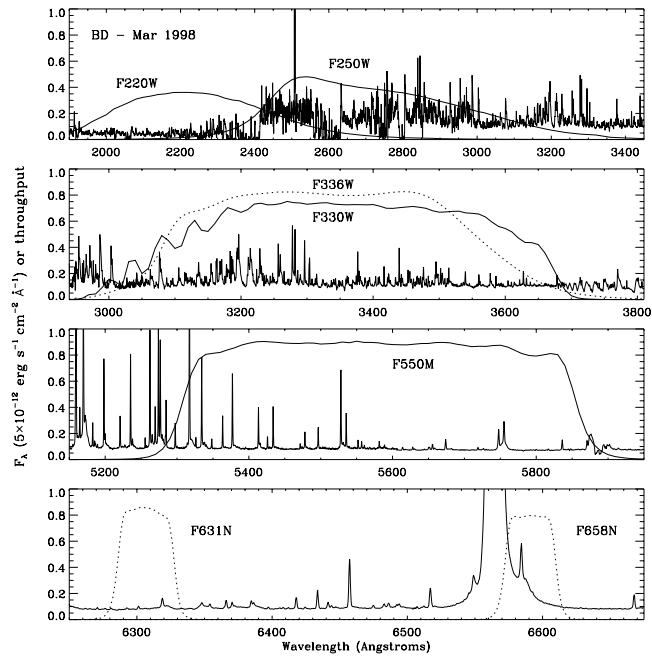
FIG. 14.—System throughput for each of the *HST* imaging filters compared with the combined *HST* STIS spectrum of the Weigelt objects B and D obtained in 1998 March when η Car was in the low-excitation state just after a spectroscopic event. Solid curves are for ACS (and FOC) filters, and dotted curves are for WFPC2 filters. Filter throughput is plotted on a scale of 0–1 (for the spectrum of the Weigelt objects, multiply by 5×10^{-12} ergs s^{-1} cm^{-2} Å^{-1}).

A1. THE CENTRAL STAR

Figures 12 and 13 show STIS spectra of the star in 1998 March and 2000 March, respectively, using a $0\farcs1 \times 0\farcs13$ aperture with the long slit oriented at a position angle close to the polar axis of the Homunculus. These are meant to represent the star's spectrum in the low- and high-excitation phases of the 5.5 yr spectroscopic cycle. The primary reason for including direct spectra of the star is for comparison with the spectra of other positions around η Car that are discussed below, which include reflected starlight. However, some details are worth mentioning here; Hillier et al. (2001) presented a detailed analysis of the central star's spectrum recorded in 1998 March.
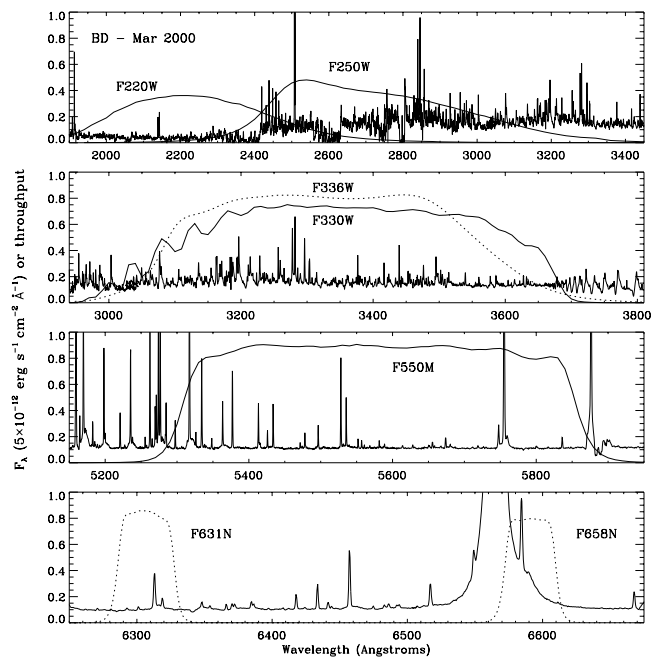

FIG. 15.—System throughput for each of the *HST* imaging filters compared with the combined *HST* STIS spectrum of the Weigelt objects B and D obtained in 2000 March when η Car was in the high-excitation state between spectroscopic events. Solid curves are for ACS (and FOC) filters, and dotted curves are for WFPC2 filters. Filter throughput is plotted on a scale of 0–1 (for the spectrum of the Weigelt objects, multiply by 5×10^{-12} ergs s^{-1} cm^{-2} Å^{-1}).

The F220W and F250W filter images trace mainly stellar continuum on either side of the absorption edge at $\sim$2400 Å but also include a rich forest of emission and absorption lines, mainly Fe II. The relative contribution from the continuum changed between 1998 and 2000, in part because of the brightening of the central star, but Figures 12 and 13 hint that interesting changes should be seen with the UV imaging filters during the spectroscopic event of 2003.5. The F336W and F330W images are nearly identical and are dominated by continuum. The strong Fe II emission features near 3200 Å contribute only a few percent of the total flux in these images. The F550M and F631N images are clearly dominated by continuum emission (except that [N II] $\lambda5755$ was stronger in 2000, still contributing less than 5% of the total flux in the F550M image). F658N includes less than half continuum emission, and the rest comes from the red wing of Hα.

A2. THE WEIGELT OBJECTS B AND D

Figures 14 and 15 show STIS spectra of the Weigelt objects B and D extracted from the same data set as the stellar spectra in Figures 13 and 14. At short wavelengths (F220W, F250W, F330W, and F336W) the observed flux recorded in the imaging filters is still dominated by continuum and reflected emission lines from the star; the contribution of narrow nebular emission lines not seen in the star's spectrum is always less than 25% of the total flux. This is even the case for the F250W filter, which includes the bright and highly variable fluorescent Fe II lines near 2500 Å (see Johansson & Letokhov 2001; Johansson & Hamann 1993; Davidson et al. 1997; Viotti et al. 1989).

The contribution of nebular emission lines to imaging filters is critical for interpreting the kinematics of the Weigelt objects discussed in § 4. In the F550M images, narrow lines contribute less than 5% of the total observed flux from the Weigelt objects, even in 2000 March when the [N II] $\lambda5755$ line was particularly strong. Similarly, [S III] $\lambda6312$ contributed only 3%-8% of the total flux in the F631N images, so both the F631N and F550M images appear to be dominated by continuum emission and are reliable indicators of proper motion. In this regard, it is surprising that [N II] $\lambda6583$ makes such a small contribution of less than 15% in the F658N images, since the motion of blob D is so anomalous in this filter. Perhaps the [N II] line makes more significant contributions at other epochs, such as 1995 and 2001, when the motion was peculiar.

The UV excess represents a substantial difference in the UV continuum level compared to other features in the Homunculus. From Figure 16 we see that the ratio of the continuum F_λ between 2500 and 5500 Å is $\sim$5, compared to values of $\sim$0.9 and $\sim$1 for the continuum in the Weigelt objects and central star, respectively, which is in qualitative agreement with the models in Figure 5b. This excess may be spatially resolved emission from large radii in the equatorial zones of the outer wind, as discussed in § 3.2, or perhaps scattered light. If it is scattered light, the much stronger 2500-to-5500 Å flux ratio is interesting, because it traces a very different line of sight to the star than our own direct view. Specifically, observations require that the bright central star be blocked by a dusty "coronograph" that allows us to see the surrounding faint nebulosity in great detail (e.g., Hillier & Allen 1992; Hillier et al. 2001). UV emission may escape more easily in the low-density equatorial regions of η Car's nonspherical wind (Smith et al. 2003a).

A3. EQUATORIAL UV EXCESS

Figure 16 shows the STIS spectrum observed 0″1–0″6 northeast of the star, associated with the UV excess demonstrated in Figures 4a and 6a. This spectrum was obtained on 2001 April 17, during the high-excitation phase of η Car. Like the Weigelt
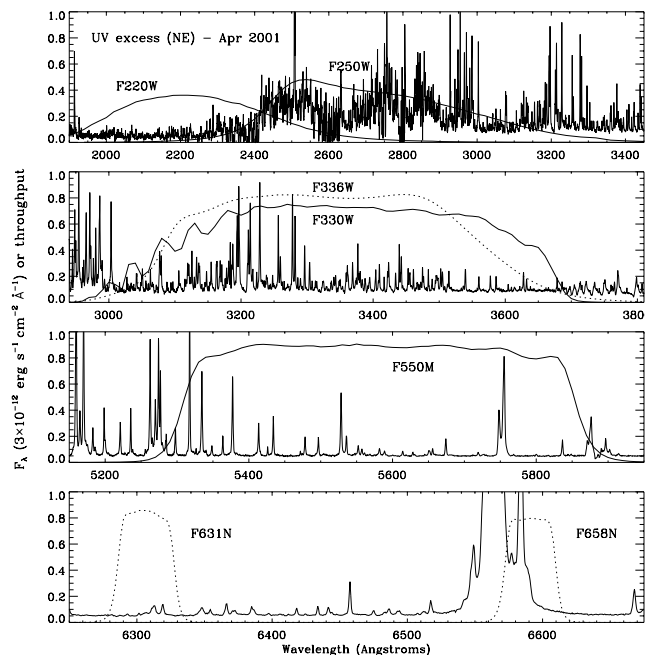

FIG. 16.—System throughput for each of the *HST* imaging filters compared with the *HST* STIS spectrum of the equatorial region 0″1–0″6 northeast of the star obtained on 2001 April 17 when η Car was in the high-excitation state between spectroscopic events. Solid curves are for ACS (and FOC) filters, and dotted curves are for WFPC2 filters. Filter throughput is plotted on a scale of 0–1 (for the spectrum of the equatorial emission, multiply by 3×10^{-12} ergs s^{-1} cm^{-2} Å^{-1}).

objects, this spectrum is a mix of reflected starlight and nebular emission. Interestingly, at optical wavelengths the relative contribution of nebular lines is stronger than in the Weigelt objects, while at UV wavelengths it is weaker compared to the continuum level. The [N II] $\lambda 6583$ line contributes roughly half the flux in the F658N image, with the rest due to reflected continuum and redshifted Hα. The [S III] $\lambda 6312$ and Fe II $\lambda 6317$ lines are roughly equal, together contributing $\sim 20\%$ of the flux in the F631N image at this epoch. Numerous nebular lines make significant but not dominant contributions to the F550M, F330W, and F336W images, while continuum clearly dominates the flux in the F220W and F250W images.

Thus, while equatorial nebular emission makes a significant contribution at optical wavelengths where the variability is conspicuous in narrowband images (Smith et al. 2000), we conclude that *the equatorial UV excess emission seen with broad UV imaging filters is due primarily to continuum and broad-line emission from the stellar wind*. This is consistent with the tracings in Figure 4a, which show the strongest excess emission in the F220W and F250W images, whereas the relative contribution of equatorial emission from F330W and F550M is less. It is also consistent with expectations from our stellar wind models in Figure 5b. Contrast this situation with that of the Purple Haze (see below), where the excess is due to nebular lines and all three of the F220W, F250W, and F330W images show a comparable excess.

A4. THE PURPLE HAZE

Figure 17 shows a segment of the long-slit spectrum observed $\sim 1\rlap{.}''6$ northwest of the star in the Purple Haze, obtained with STIS in 2001 November (the slit aperture was oriented nearly perpendicular to the polar axis of the Homunculus). A forest of nebular lines (at positions $\pm 1''$ in Fig. 17) are seen superposed on much fainter reflected near-UV continuum light from the star. At least 60% of the total integrated flux in the F330W and F336W images is from nebular emission lines. This is roughly the same amount as the excess emission in the F330W image compared to the F550M image at $1\rlap{.}''6$ northwest in Figure 4b. Thus, the excess emission that causes the Purple Haze in all imaging filters is *dominated by nebular emission lines instead of scattered light* (see also Zethson et al. 1999). This emission probably originates in the receding northwest polar lobe of the Little Homunculus (see § 3.3 and Fig. 7), and blueshifted filaments emitting [Sr II] and other low-ionization lines are seen along the same line of sight (Zethson et al. 2001; Hartman et al. 2004). Zethson et al. (1999) observed multiple velocity components in the Fan region, and Smith (2002) noted that with a revised inclination of $i \approx 42°$, these various velocity components were consistent with equatorial ejecta originating in *both* the Great Eruption of 1843 and the 1890 outburst (see also Davidson et al. 2001). So far, only *equatorial* gas is seen to be conspicuously variable in the images, relevant to some interpretations of the stellar-wind structure and variability mentioned above (Smith et al. 2003a).

APPENDIX B

DETAILS OF PROPER-MOTION DISCREPANCIES

Very recently, Dorland, Currie, & Hajian (2004) have also investigated the proper motion of the Weigelt objects C and D using *HST* WFPC2 images, and those authors suggest that the Weigelt objects were ejected around 1940, perhaps associated with the brightening event seen in η Car's light curve around that time. This differs from our conclusion that the Weigelt objects were likely ejected in the 1890 event and accelerated somewhat so that proper motions give a slightly later ejection date around 1908 (see § 4). Although these conclusions are very different, one could argue that there is no discrepancy in the actual measurements—only the interpretations—since Dorland et al.'s quoted ejection date for object D ($1934.1^{+16.0}_{-31.7}$) is consistent with ours (1907 ± 12) within the stated uncertainty. (Note that Dorland et al.'s measurements are based on shorter time baselines—5.9 yr for D and 1.7 yr for C than our baseline of ~ 9 yr for both D and C.) Nevertheless, it may be worthwhile to briefly examine differences between our
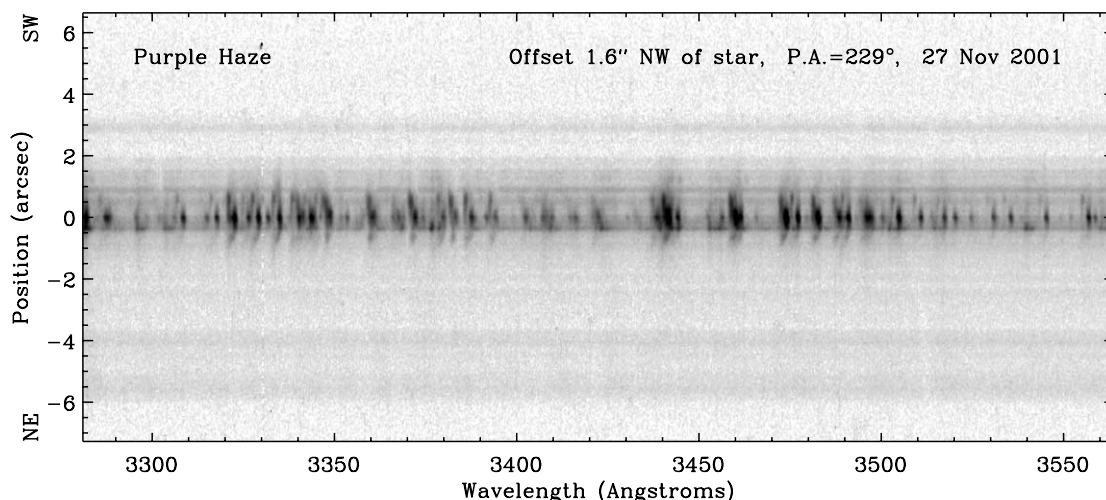

FIG. 17.—Example section of the long-slit *HST* STIS spectrum of the Purple Haze. The slit was positioned $1\rlap{.}''6$ northwest of the central star at P.A. $= 229°$. The bright nebular emission features of the Purple Haze can be seen within $\pm 1''$ of zero, whereas the scattered continuum spectrum of the star can be seen as far as $-6''$ (to the northeast). This is just one small but representative segment of the spectrum.

two proper-motion estimates, since the corresponding interpretations they lead to are mutually exclusive. Below we discuss three critical differences between our measurements that could significantly affect the age determination for the Weigelt objects.

Contamination from emission lines.—Dorland et al. (2004) based their analysis mainly on *HST* WFPC2 images with the narrowband F658N filter, transmitting [N II] λ6583 (they also used the F631N filter, but only over a 1.7 yr baseline). We have shown that F658N filter images are not a reliable indicator of proper motion for the Weigelt objects: for example, D appears to move *backward* (i.e., toward the star) between 1995 and 1997. This is probably because higher ionization lines such as [N II] are formed in an ablated halo around their dusty cores and therefore trace different kinematics (see § 4.6). Lines such as [N II] are also sensitive to severe ionization changes during η Car's 5.5 yr spectroscopic cycle (Damineli et al. 1998).

Subpixel Sampling.—The 0″.0455 pixel scale of WFPC2 PC images is a substantial fraction of the separation between the central star and the Weigelt objects, and the transverse motions being measured are only a fraction of a PC pixel. We have used image dithering and subpixel resampling techniques to improve our limiting spatial resolution to better isolate the condensations. We have confidence in our techniques, because our resampled PC images appear very similar to the ACS/HRC images obtained with a raw pixel scale almost twice as small as the original PC pixel scale. Our WFPC2 PC and ACS/HRC proper-motion measurements in 2002−2003 (Fig. 11) agree very well, using both rotated and nonrotated images. However, in their analysis, Dorland et al. (2004) measured motions using the raw WFPC2 PC pixel sampling. This lower effective spatial resolution may result in different measured motions for the Weigelt objects in the crowded region immediately surrounding the central star. For example, Figure 8*d* shows Dorland et al.'s quoted position for D (*cross*) superposed on contours of an ACS/HRC image of η Car. We see that Dorland et al.'s measured position is measurably farther from the star (inferring faster motions) than the peak emission from blob D in the ACS/HRC image. Figure 8*d* also shows two condensations slightly farther from the star than D to the north and northwest. Smith et al. (2000) showed that between 1995 and 1999 these more distant condensations brightened more than the Weigelt objects, which could bias the centroid position of D radially outward if it were not spatially resolved from these condensations.

Median Filtering.—Finally, the proper-motion estimates of Dorland et al. (2004) differed from ours in the actual method of measuring the positions of the emission knots. We based our analysis on the average of three different measurement techniques (two-dimensional Gaussian radial profile, one-dimensional tracings, and flux-weighted centroid) applied to the final flux-calibrated images, whereas Dorland et al. used a two-dimensional Gaussian applied to median-subtracted images. These median-subtracted images were produced by making a smoothed median image with a 0″.23 × 0″.23 kernel and subtracting it from the raw flux image. While this method is useful for enhancing contrast in faint structures around bright stars, it can also artificially shift the position of a faint emission feature farther from the star, since more flux can be subtracted from the star-facing side of the knot. We checked this effect in our own images by measuring the positions of C and D using a flux-weighted centroid on median-subtracted images with the same kernel size as used by Dorland et al. (see Table 3). The variance between the median-subtracted and raw images indicated an average shift of +5 mas farther from the star in the median-subtracted images (in every case the separation was larger in the median-subtracted measurements). While the shift is not enough to account fully for the discrepancy between our measured positions and those of Dorland et al., it is in the right direction, and the effect could be more severe in images with larger pixels such as those used by Dorland et al. Perhaps all three of the differences discussed here conspire to make Dorland et al.'s measurements different from ours; in that case, continued monitoring of the proper motions of the Weigelt objects will be useful for determining their true age.

REFERENCES

Corcoran, M. F., Ishibashi, K., Swank, J. H., Davidson, K., Petre, R., & Schmitt, J. H. M. M. 1997, Nature, 390, 587
Corcoran, M. F., Ishibashi, K., Swank, J. H., & Petre, R. 2001, ApJ, 547, 1034
Currie, D. G., et al. 1996, AJ, 112, 1115
Damineli, A. 1996, ApJ, 460, L49
Damineli, A., Conti, P. S., & Lopes, D. F. 1997, NewA, 2, 107
Damineli, A., Stahl, O., Kaufer, A., Wolf, B., Quast, G., & Lopes, D. F. 1998, A&AS, 133, 299
Davidson, K. 1997, NewA, 2, 387
———. 1999, in ASP Conf. Ser. 179, Eta Carinae at the Millenium, ed. J. A. Morse, R. M. Humphreys, & A. Damineli (San Francisco: ASP), 304
Davidson, K., Ebbets, D., Weigelt, G., Humphreys, R. M., Hajian, A. R., Walborn, N. R., & Rosa, M. 1995, AJ, 109, 1784
Davidson, K., & Humphreys, R. M. 1997, ARA&A, 35, 1
Davidson, K., Smith, N., Gull, T. R., Ishibashi, K., & Hillier, D. J. 2001, AJ, 121, 1569
Davidson, K., et al. 1997, AJ, 113, 335
Dorland, B. N., Currie, D. G., & Hajian, A. R. 2004, AJ, in press
Duncan, R. A., & White, S. M. 2003, MNRAS, 338, 425
Duschl, W. J., Hofmann, K. H., Rigaut, F., & Weigelt, G. 1995, Rev. Mexicana Astron. Astrofis. Ser. Conf., 2, 17
Ebbets, D. C., Walborn, N. R., & Parker, J. W. 1997, ApJ, 489, L161
Falcke, H., Davidson, K., Hofmnn, K. H., & Weigelt, G. 1996, A&A, 306, L17
Gaviola, E. 1950, ApJ, 111, 408
Gehrz, R. D., & Ney, E. P. 1972, S&T, 44, 4
Gull, T. R., & Ishibashi, K. 2001, in ASP Conf. Ser. 242, Eta Carinae and Other Mysterious Stars: The Hidden Opportunities of Emission Line Spectroscopy, ed. T. R. Gull, S. Johansson, & K. Davidson (San Francisco: ASP), 59
Gull, T. R., Ishibashi, K., Davidson, K., & Collins, N. 2001, in ASP Conf. Ser. 242, Eta Carinae and Other Mysterious Stars: The Hidden Opportunities of Emission Line Spectroscopy, ed. T. R. Gull, S. Johansson, & K. Davidson (San Francisco: ASP), 391

Hackwell, J. A., Gehrz, R. D., & Grasdalen, G. L. 1986, ApJ, 311, 380
Hamann, F., DePoy, D. L., Johansson, S., & Elias, J. 1994, ApJ, 422, 626
Hartman, H., Gull, T. R., Johansson, S., Smith, N., & The HST Eta Car Treasury Team 2004, A&A, in press
Hillier, D. J., & Allen, D. A. 1992, A&A, 262, 153
Hillier, D. J., Davidson, K., Ishibashi, K., & Gull, T. R. 2001, ApJ, 553, 837
Hillier, D. J., & Miller, D. L. 1998, ApJ, 496, 407
Hofmann, K. H., & Weigelt, G. 1988, A&A, 203, L21
Humphreys, R. M., Davidson, K., & Smith, N. 1999, PASP, 111, 1124
Iping, R., Sonneborn, G., Gull, T. R., & Massa, D. 2001, in ASP Conf. Ser. 242, Eta Carinae and Other Mysterious Stars: The Hidden Opportunities of Emission Line Spectroscopy, ed. T. R. Gull, S. Johansson, & K. Davidson (San Francisco: ASP), 55
Ishibashi, K., Corcoran, M. F., Davidson, K., Swank, J. H., Petre, R., Drake, S. A., Damineli, A., & White, S. 1999, ApJ, 524, 983
Ishibashi, K., et al. 2003, AJ, 125, 3222
Johansson, S., & Hamann, F. W. 1993, Phys. Scr., T47, 157
Johansson, S., & Letokhov, V. S. 2001, A&A, 378, 266
Lucy, L. 1974, AJ, 79, 745
Meaburn, J., Gehring, G., Walsh, J. R., Palmer, J. W., Lopez, J. A., Bruce, M., & Raga, A. C. 1993, A&A, 276, L21
Meaburn, J., Wolstencroft, R. D., & Walsh, J. R. 1987, A&A, 181, 333
Monnier, J. D., Tuthill, P. G., & Danchi, W. C. 2002, ApJ, 567, L137
Morris, P. W., et al. 1999, Nature, 402, 502
Morse, J. A., Davidson, K., Bally, J., Ebbets, D., Balick, B., & Frank, A. 1998, AJ, 116, 2443
Morse, J. A., Kellogg, J. R., Bally, J., Davidson, K., Balick, B., & Ebbets, D. 2001, ApJ, 548, L207
Richardson, W. H. 1972, J. Opt. Soc. Am., 62, 55
Rigaut, F., & Gehring, G. 1995, Rev. Mexicana Astron. Astrofis. Ser. Conf., 2, 27
Ringuelet, A. E. 1958, Z. Astrophys., 46, 276

Schulte-Ladbeck, R. E., Pasquali, A., Clampin, M., Nota, A., Hillier, D. J., & Lupie, O. L. 1999, AJ, 118, 1320
Smith, C. H., et al. 1995, MNRAS, 273, 354
Smith, N. 2002, MNRAS, 337, 1252
Smith, N., Davidson, K., Gull, T. R., Ishibashi, K., & Hillier, D. J. 2003a, ApJ, 586, 432
Smith, N., & Gehrz, R. D. 1998, AJ, 116, 823
———. 2000, ApJ, 529, L99
Smith, N., Gehrz, R. D., Hinz, P. M., Hoffmann, W. F., Hora, J. L., Mamajek, E. E., & Meyer, M. R. 2003b, AJ, 125, 1458
Smith, N., Gehrz, R. D., Hinz, P. M., Hoffmann, W. F., Mamajek, E. E., Meyer, M. R., & Hora, J. L. 2002, ApJ, 567, L77
Smith, N., Gehrz, R. D., & Krautter, J. 1998, AJ, 116, 1332
Smith, N., Morse, J. A., Davidson, K., & Humphreys, R. M. 2000, AJ, 120, 920
Thackeray, A. D. 1949, Observatory, 69, 31
———. 1961, Observatory, 81, 99
Tuthill, P. G., Monnier, J. D., & Danchi, W. C. 1999, Nature, 398, 487
Verner, E. M., Gull, T. R., Bruhweiler, F., Johansson, S., Ishibashi, K., & Davidson, K. 2002, ApJ, 581, 1154

Viotti, R., Rossi, L., Cassatella, A., Altmore, A., & Baratta, G. B. 1989, ApJS, 71, 983
Visvanathan, N. 1967, MNRAS, 135, 275
Walborn, N. R. 1976, ApJ, 204, L17
Walborn, N. R., Blanco, B. M., & Thackeray, A. D. 1978, ApJ, 219, 498
Walborn, N. R., & Liller, M. 1977, ApJ, 211, 181
Weigelt, G., & Ebersberger, J. 1986, A&A, 163, L5
Weigelt, G., et al. 1995, Rev. Mexicana Astron. Astrofis. Ser. Conf., 2, 11
Whitney, C. A. 1952, Harvard Obs. Bull., 921, 8
Williams, P. M., van der Hucht, K. A., Pollock, A. M. T., Florkowski, D. R., van der Woerd, H., & Wamsteker, W. M. 1990, MNRAS, 243, 662
Zanella, R., Wolf, B., & Stahl, O. 1984, A&A, 137, 79
Zethson, T. 2001, Ph.D. thesis, Univ. Lund
Zethson, T., Gull, T. R., Hartman, H., Johansson, S., Davidson, K., & Ishibashi, K. 2001, AJ, 122, 322
Zethson, T., Johansson, S., Davidson, K., Humphreys, R. M., & Ishibashi, K. 1999, A&A, 344, 211